

The PAU Survey:

Enhancing photometric redshift estimation using DEEPz

I. V. Daza-Perilla^{1,2,3}, M. Eriksen^{4,5}, D. Navarro-Gironés^{6,7}, E. J. Gonzalez^{3,4}, F. Rodriguez^{1,3}, E. Gaztañaga^{6,7,8}, C. M. Baugh⁹, M. Lares¹, L. Cabayol-Garcia^{4,5}, F. J. Castander^{6,7}, M. Siudek^{6,10}, A. Wittje¹¹, H. Hildebrandt¹¹, R. Casas^{6,7}, P. Tallada-Crespi^{5,12}, J. Garcia-Bellido¹³, E. Sanchez¹², I. Sevilla-Noarbe¹², R. Miquel^{4,14}, C. Padilla⁴, P. Renard¹⁵, J. Carretero^{5,12}, and J. De Vicente¹²

¹ Instituto de Astronomía Teórica y Experimental (IATE), CONICET-UNC, Córdoba, X5000BGR, Argentina

² Facultad de Matemática, Astronomía, Física y Computación, Universidad Nacional de Córdoba (UNC), Córdoba, CP:X5000HUA, Argentina

³ Observatorio Astronómico de Córdoba, Universidad Nacional de Córdoba, Laprida 854, Córdoba, X5000BGR, Argentina

⁴ Institut de Física d'Altes Energies (IFAE), The Barcelona Institute of Science and Technology, Campus UAB, 08193 Bellaterra (Barcelona), Spain

⁵ Port d'Informació Científica (PIC), Campus UAB, C. Albareda s/n, 08193 Bellaterra (Barcelona), Spain

⁶ Institute of Space Sciences (ICE, CSIC), Campus UAB, Carrer de Can Magrans, s/n, 08193 Barcelona, Spain

⁷ Institut d'Estudis Espacials de Catalunya (IEEC), E-08034 Barcelona, Spain

⁸ Institute of Cosmology & Gravitation, University of Portsmouth, Dennis Sciamia Building, Burnaby Road, Portsmouth PO1 3FX, UK

⁹ Institute for Computational Cosmology, Department of Physics, South Road, Durham, DH1 3LE, UK

¹⁰ Instituto Astrofísica de Canarias, Av. Via Lactea s/n, E38205 La Laguna, Spain

¹¹ Ruhr University Bochum, Faculty of Physics and Astronomy, Astronomical Institute (AIRUB), German Centre for Cosmological Lensing, 44780 Bochum, Germany

¹² Centro de Investigaciones Energéticas, Medioambientales y Tecnológicas (CIEMAT), Avenida Complutense 40, E-28040 (Madrid), Spain

¹³ Instituto de Física Teórica (UAM/CSIC), Nicolas Cabrera 13, Cantoblanco, E-28049 (Madrid), Spain

¹⁴ Institució Catalana de Recerca i Estudis Avançats (ICREA), 0810 Barcelona, Spain

¹⁵ Department of Astronomy, Tsinghua University, Beijing 100084, China

Received September 15, 1996; accepted March 16, 1997

ABSTRACT

We present photometric redshifts for 1 341 559 galaxies from the Physics of the Accelerating Universe Survey (PAUS) over 50.38 deg² of sky to $i_{AB} = 23$. Redshift estimation is performed using DEEPz, a deep-learning photometric redshift code. We analyse the photometric redshift precision when varying the photometric and spectroscopic samples. Furthermore, we examine observational and instrumental effects on the precision of the photometric redshifts, and we compare photometric redshift measurements with those obtained using a template method-fitting BCNz2. Finally, we examine the use of photometric redshifts in the identification of close galaxy pairs. We find that the combination of samples from W1+W3 in the training of DEEPz significantly enhances the precision of photometric redshifts. This also occurs when we recover narrow band fluxes using broad bands measurements. We show that DEEPz determines the redshifts of galaxies in the prevailing spectroscopic catalogue used in the training of DEEPz with greater precision. For the faintest galaxies ($i_{AB} = 21 - 23$), we find that DEEPz improves over BCNz2 both in terms of the precision (20-50 per cent smaller scatter) and in returning a smaller outlier fraction in two of the wide fields. The catalogues were tested for the identification of close galaxy pairs, showing that DEEPz is effective for the identification of close galaxy pairs for samples with $i_{AB} < 22.5$ and redshift $0.2 < z < 0.6$. In addition, identifying close galaxy pairs common between DEEPz and BCNz2 is a promising approach to improving the purity of the catalogues of these systems.

Key words. galaxies: distances and redshifts – techniques: photometric – methods: data analysis

1. Introduction

The estimation of photometric redshifts is a fundamental task for numerous objectives in cosmology. They enable the mapping of the Universe's large-scale structure and the study of the physical properties of galaxies (e.g., Jarrett 2004; Tanaka & Kodama 2004). These redshifts also allow the exploration of the Universe's evolution throughout its history, contributing to the

validation and improvement of cosmological models, including the study of dark matter and dark energy (Weinberg et al. 2013; Survey et al. 2023). Improving the precision of photometric redshifts is crucial for creating comprehensive catalogues, which in turn enhances the quality and validity of scientific studies based on these redshift data. It also aids in decision-making for observational plans and survey strategies. Achieving high precision in redshifts, for a large number of observations, and over a signifi-

cant volume of data sampled simultaneously remains a challenge both for spectroscopic and imaging surveys (Hildebrandt et al. 2010; Salvato et al. 2019).

Spectroscopic surveys are a valuable source of high-precision redshifts; however, this approach is limited by the number of observations that can be carried out within a specific volume, the time needed to acquire high-quality spectra as well as the challenges associated with studying bright galaxies at low redshifts and faint galaxies at high redshifts. Additionally, selection based on galaxy colour also contributes to these limitations. All these constraints make the generation of spectroscopic catalogues in extensive and uniform volumes difficult. However, the Dark Energy Spectroscopic Instrument (DESI) has created the largest 3D map of the universe ever made and measured the rate at which the universe expanded 8-11 billion years ago with a precision of 1 percent, providing a powerful way to study dark energy (DESI Collaboration et al. 2024).

On the other hand, imaging surveys with several filter bands can provide denser galaxy samples over larger volumes by going deeper than spectroscopic surveys, but with lower precision redshifts. The precision of redshifts obtained from a handful of broad bands (BB) is typically ~ 0.05 , measured from the distribution of relative differences between the spectroscopic redshift, z_s , and the photometric redshift, z_p , expressed as $\Delta z \equiv (z_p - z_s)/(1 + z_s)$ (Hildebrandt et al. 2012; Hoyle et al. 2018). To enhance the precision in estimating z_p , it is necessary to have a higher resolution over the wavelength range of the spectral energy distribution (SED). Several surveys have therefore incorporated medium and narrow-band filters to obtain improved photometric redshifts (Martí et al. 2014; Molino et al. 2020), such as the Advanced Large Homogeneous Area Medium Band Redshift Survey (ALHAMBRA, Molino et al. 2014), the Javalambre Physics of the Accelerating Universe Survey (J-PAS, Benítez et al. 2014), the High-redshift and Dead Sources Redshift Survey (SHARDS, Barro et al. 2019), the Javalambre Photometric Local Universe Survey (J-PLUS, Cenarro et al. 2019), and the Southern Photometric Local Universe Survey (S-PLUS, De Oliveira et al. 2019), as well as the Physics of the Accelerating Universe Survey used here (PAUS, Padilla et al. 2019).

The PAUS data can be used to obtain high-quality photometric redshift measurements through the combination of data from 40 narrow-band photometric filters with existing, deeper BB photometry. This combination improves precision compared to estimates based solely on BB (Alarcon et al. 2021), which has a direct impact on the studies carried out with PAUS, such as measuring intrinsic alignments, galaxy clustering (Johnston et al. 2021), characterizing properties of galaxies (Tortorelli et al. 2021; Renard et al. 2022; Csizi et al. 2024), studies over galaxy evolution and formation (Manzoni et al. 2024), cosmic shear (Van Den Busch et al. 2022), and identifying close galaxy pairs (Gonzalez et al. 2023).

Different techniques have been implemented to improve and expand photometric redshift catalogues estimated using the PAUS data (Eriksen et al. 2019; Alarcon et al. 2020). Eriksen et al. (2019) introduced the BCNz2 code, which was designed specifically to handle the combination of 40 narrow filters and broadband filters from PAUS and Subaru, obtained as part of the COSMOS-20 survey (Taniguchi et al. 2015). The BCNz2 code fits templates to the observed fluxes and provides z_p in the COSMOS field with a high level of precision, which is inferred by comparing to available spectroscopic redshifts. The measured precision is ~ 0.0037 for the 50 per cent of all galaxies adjudged to have the highest quality photometric redshift (in terms of the quality factor, see Eriksen et al. 2019) with magnitudes

$i_{AB} < 22.5$ and measured redshifts $z_s < 1.2$. Alarcon et al. (2020) extended the development of a hierarchical Bayesian model to estimate redshifts. This method has been tested on realistic simulations, showing that the incorporation of galaxy clustering information improves redshift determinations and reduces systematic redshift uncertainties.

Eriksen et al. (2020) implemented DEEPz, a deep learning code that includes simulations in the initial training phase and is then trained on observational data. As a result, DEEPz reduced the σ_{68} dispersion statistic by 50 per cent at $i_{AB} = 22.5$ compared to existing algorithms in the COSMOS field.

The aim of this work is to determine z_p in wide fields of PAUS with DEEPz, a method that has not been implemented in these fields. This study also investigates the observational and instrumental effects that may vary between photometric and spectroscopic surveys and the wide PAUS fields on the precision of z_p estimates up to apparent magnitudes $i_{AB} = 23$, and to compare our z_p measurements with those presented in Navarro-Gironés et al. (2023) using the BCNz2 method, as both methodologies are affected by different issues. In the case of template methods, it is expected that z_p catalogues will exhibit significant dispersion and low precision at high redshifts, whereas machine-learning based methods are occasionally affected by oversampling. Additionally, we investigate whether these catalogues can be implemented in studies such as the identification of close galaxy pairs.

The article is organised as follows. Section 2 provides an overview of the observational and simulated data used in each field. Section 3 introduces the DEEPz model used for determination of the z_p catalogues and outlines the metrics used to evaluate the z_p performance. In this section, we also present the description of the various tests conducted to generate accurate photometric redshifts in three observed wide-fields. Sect. 4 we present the obtained z_p for each field and the combination of them. We analyse the variation in the precision of z_p according to instrumental and observational effects, and the spectroscopic sample used in the training of DEEPz. Additionally, it assesses the performance of z_p in identifying galaxy pairs and compares the results obtained with DEEPz and BCNz2 and we describe the generation of the catalogues in each field. Sect. 5 we implement the z_p in the identification of close galaxy pairs. Finally, Section 6 summarises the conclusions of this work.

Throughout, we adopt a Planck 2015 cosmology (Ade et al. 2016) with the following parameters: $H_0 = 67.3 \text{ km s}^{-1} \text{ Mpc}^{-1}$, $\Omega_m = 0.315$, and $\Omega_\Lambda = 0.685$.

2. Data

Here, we calculate photometric redshift values in three wide fields observed by PAUS, labelled as W1, W3, and G09 (see fig. 1). To estimate z_p in each field, we used a combination of simulated and observational data. The observational data is comprised of individual exposures, coadded fluxes from 40 narrow bands of PAUS (NB), and spectroscopic redshifts from various surveys. The specific data used depends on the area under consideration, as set out below.

2.1. PAUS data

The PAUS catalogues have been meticulously crafted by the Port d'Informació Científica (PIC) data centre. The catalogues are derived from 40 NB optical images, which were acquired with the PAUCam instrument on the William Herschel Telescope at the Observatorio del Roque de los Muchachos in La Palma, Ca-

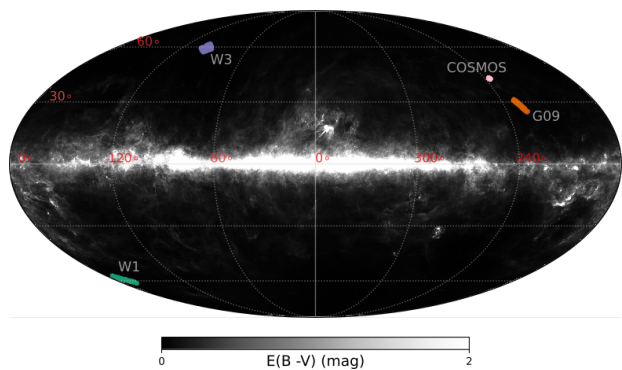


Fig. 1. Aitoff Galactic Projection, showing the location of the PAUS fields and the Galactic extinction. The level of extinction is shown in terms of the $E(B - V)$ parameter on a linear scale, as shown by the key. The data are from the dust map provided by the Planck Collaboration (Aghanim et al. 2016). The W1, G09, W3 and COSMOS wide-fields are shown in green, orange, violet, and pink, respectively.

nary Islands (Padilla et al. 2019; Castander et al. 2012). The data spans the wavelength range from 4500 Å to 8500 Å, with a uniform spacing of 100 Å between contiguous bands, giving an average spectral resolution of $R \sim 65$. The target fields covered by PAUS are the COSMOS field, the Canada-France-Hawaii Telescope Legacy Survey CFHTLS fields (W1, W3 and W4), and the KiDS/GAMA G09 field (Heymans et al. 2012; Erben et al. 2013; Tortorelli et al. 2021). PAUS has covered 12.04 deg² in W1, 15.7 deg² in G09, 22.64 deg² in W3, and 1 deg² in the COSMOS field. PAUS has performed only a few observations in the W4 field, so we have not included this here. Fig. 1 shows, in the Galactic Aitoff projection, the location of these four fields, along with the dust distribution provided by Planck (Aghanim et al. 2016).

The data reduction and galaxy photometry are obtained through two pipelines, the primary pipeline, referred to as the nightly pipeline, which handles all the image processing, with customised algorithms used for photometric calibration (Castander et al. 2024; Serrano et al. 2022). The multi-epoch and multi-band analysis (MEMBA) pipeline performs forced photometry on a reference catalogue to optimise photometric redshift performance.

2.2. W1 Field

The CFHTLS-WIDE observations cover four patches of the sky at high Galactic latitudes, and are made up of pointings of $1^\circ \times 1^\circ$ (Erben et al. 2013). The W1 field has 72 pointings centred on RA = 02^h18^m00^s, DEC = -07^d00^m00^s. In this field, the PAUS coadded fluxes of 40 NBs correspond to the MEMBA production 1015 and are produced using inverse variance weighting of the individual measurements. Some of these sources have several individual exposures in a single band reaching a maximum of 11 observations. However, most of them have only one observation. We used the CFHTLenS data set for the BB in five filters u^* , g' , r' , i' , z' for sources with `star_flag` = 0.

The spectroscopic redshift sample used to train DEEPz in this field is made up of data from 13 catalogues. Approximately 60% of the spectroscopic data used is derived from the VIMOS Public Extragalactic Redshift Survey (VIPERS, Guzzo et al. 2014; Garilli et al. 2014). VIPERS covers a total area of approximately 24deg² located within the CFHTLS-Wide W1 and W4 fields and is limited to objects with magnitudes $i_{AB} < 22.5$ and redshifts in the range of $0.5 < z < 1.5$. The other half of the spectro-

scopic data, which we will refer to as GAMA-SDSS from now on, comes from various sources, with the Galaxy and Mass Assembly GAMA (Driver et al. 2009, 2011; Baldry et al. 2018) catalogue being one of the most significant contributors. GAMA has obtained redshifts for a quarter of a million galaxies, primarily using the 2dF/AAOmega instrument on the Anglo-Australian Telescope. The final data are described in Liske et al. (2015), with GAMA achieving a high completeness (better than 98%) down to $r_{AB} < 19.8$ over an area of 180 deg² in the equatorial G09, G12, and G15 fields (60 deg² each). The W1 field represents 20 per cent of the total sample. The Sloan Digital Sky Survey Data Release 16 SDSS-DR16 (Ahumada et al. 2020) contributes approximately 13 per cent of the dataset, and the following catalogues provide the remaining information: VANDELS (Garilli et al. 2021), KBSS-MOSFIRE (Steidel et al. 2014), VVDS (Le Fèvre et al. 2013), DES_AAOMEGA (Childress et al. 2017), 3DHST (Brammer et al. 2012), DES_IMACS (Dressler et al. 2011), ZFIRE (Nanayakkara et al. 2016), C3R2 (Masters et al. 2019), and CDB (Sullivan et al. 2010).

2.3. W3 Field

The W3 field is centred on RA = 14^h17^m54^s, DEC = +01^d19^m00^s, with 49 pointings covering a total area of approximately 30 deg². Similar to the W1 field, we utilise information from the 40 PAUS NBs (production 1012), along with the five CFHTLenS BB.

In this field, we use a total of seven spectroscopic catalogues to provide the training data. Half of the data comes from SDSS-DR16 (Ahumada et al. 2020). The bulk of the remaining data (40 per cent) is from DEEP2-DR4 (Newman et al. 2013), with a magnitude limit of $r_{AB} = 24.1$, reaching a $z = 1.5$. The remaining minor contributions of spectroscopic information come from 3DHST (Brammer et al. 2012), C3R2 (Masters et al. 2019), CDB (Sullivan et al. 2010), and SAGA (Geha et al. 2017).

2.4. G09 Field

The PAUS team conducted observations in a limited portion of the CFHTLS-W2 patch, focusing on 33 pointings centred on the coordinates RA 08^h54^m00^s and DEC -04^d15^m00^s. This area is located within one of the four equatorial regions mapped by the GAMA survey, namely, 9h (G09), which has been documented in various publications (Driver et al. 2011; Hopkins et al. 2013; Liske et al. 2015; Driver et al. 2016). This region is 12 × 4 deg² and is located within the footprint of the public ESO Kilo-Degree Survey and the VISTA Infrared Kilo-Degree Galaxy Survey, commonly known as KiDS and VIKING, respectively (de Jong et al. 2013; Kuijken et al. 2015; De Jong et al. 2015; Edge et al. 2013; Venemans et al. 2015; Bellstedt et al. 2020).

KiDS has obtained optical images over 1500 deg², captured using OmegaCAM on the VLT Survey Telescope (VST) in the u , g , r , and i filters. Additionally, VIKING has near-infrared coverage through the VISTA telescope in the Z , Y , J , H , and K_s bands. Consequently, galaxies in the G09 field have information in nine BB.

The GAMA survey is the primary source of spectroscopic information in this area, contributing 80 per cent of the total. The remaining spectroscopic information comes from SDSS. The objects in this field that form the training sample reach apparent magnitudes of $i_{AB} = 22$.

A complementary sample called KiDz-COSMOS, extracted from the KiDS DR5 (Wright et al., in press), has been created,

containing information in the nine KiDS and VIKING bands, reaching an apparent magnitude of $i_{AB} = 22.5$. Most of the spectroscopic information in this sample comes from the extensive redshift study known as zCOSMOS-bright (Lilly et al. 2009), which covers 1.7deg^2 down to $i_{AB} = 22.5$ and $0.1 < z < 1.2$ and is a sub-sample of G10-COSMOS (Davies et al. 2015).

2.5. Subsamples

To evaluate the precision of the z_p determined by DEEPz, which incorporates supervised machine learning models, we have divided the galaxies with spectroscopic information into three random groups. One of them is used to train the models (the training set), another group is used to evaluate the model performance (the validation set), and a third (the test set) is not used in previous steps, but is reserved to estimate how precise the z_p will be for galaxies lacking spectroscopic information.

In Table 1 we show the size of the sets, i.e. the total sample and the training, validation and test sets. The first four columns are the number of galaxies in each field. The last two columns present the data augmentation, specifically the training, validation, and test samples are combined based on their similar photometric characteristics. This augmentation was applied to the W1 and W3 fields from the CFHTLenS survey, which includes (BB) photometry, as well as to a combined dataset from the G09 and COSMOS fields, which integrates BB information from the KiDS and VIKING surveys.

2.6. Simulations

The estimation of photometric redshifts by DEEPz uses a combination of observational and simulated data, as explained in the next section (Eriksen et al. 2020). Reproducing the methodology of DEEPz, we have included the code for simulating galaxy spectral energy distributions from flexible stellar population synthesis (FSPS) (Conroy et al. 2009; Conroy & Gunn 2010) in the neural network training before the input of observational data. This code uses stellar population synthesis (SPS) models to estimate stellar masses, mean ages, metallicities, and star formation histories for different star formation histories. The simulations are generated using the same parameter ranges described in Section 3.2.2 of Eriksen et al. (2020). Therefore, the samples in the W1 and W3 fields are identical to those used in that work, consisting of a thousand galaxies uniformly selected with redshift information, as well as fluxes in the PAUS NBs and in the BB of the CFHTLenS survey. Regarding the simulation of the same number of galaxies in the G09 field, the same parameter selection is used. However, in this case the FSPS code is extended to include the nine KiDS and VIKING filters (de Jong et al. 2013; Kuijken et al. 2015; De Jong et al. 2015; Edge et al. 2013; Venemans et al. 2015), and the redshift range is extended from 1.5 to 2.1.

3. Methodology

The precision of studies conducted using a statistical tool like machine learning depends on several factors: the model, the information available, in particular the amount and quality of the data provided to the model. Among the various factors that influence the performance of the model and, therefore, the determination of photometric redshifts, we have studied in each field the impact of refining the data on the photometric redshifts. In Sect. 3.1, we describe the DEEPz code. Then, in Sect. 3.2, we specify the met-

rics used to study the quality of photometric redshifts. Finally, in Sect. 3.3, we present the tests of data refinement.

3.1. DEEPz

DEEPz was designed for photometric redshift estimation in the PAU survey, using NB and BB data (Eriksen et al. 2020). Its effectiveness has been tested in the COSMOS field using photometry from the 40 NBs of the PAU survey, the BB of Subaru, and the u -band of CFHTLenS.

The methodology of DEEPz involves implementing an architecture composed of three neural networks: the first two make up an autoencoder and the third is a mixture density network (MDN). Fig. 2 shows the network flow diagram. The autoencoder is used to extract features without prior knowledge of the redshift and to improve performance for faint sources. The latent variables encoded by the autoencoder, along with the original input fluxes divided by the target band, are fed into the MDN, where the target band is defined independently for each BB survey. In the case of CFHTLenS, the target band is the i -band, while for KiDS, it is the r -band. The third neural network, the MDN gives the probability distribution of the photometric redshift. The mode of this distribution is z_p for a specific galaxy. In detail, the network architecture consists of an autoencoder with 10 layers and 250 nodes in both the encoder and decoder. Each layer includes linear transformations followed by ReLU non-linearities, batch normalization, and a 2% dropout, except for the last three layers. The autoencoder is fed galaxy flux ratios. The z_p network, which follows the same structure as the autoencoder, takes both the galaxy flux ratios and autoencoder features as input. It includes 1% dropout after all linear layers. This network is a MDN, representing the redshift distribution as a linear combination of 10 normal distributions.

We use pretraining to help adjust the weights of neural networks so that they can later be fine-tuned with observational data. The model training process begins with simulations. Performing this pre-training step before training with observational data reduces the scatter in z_p by 50 per cent for faint sources in terms of apparent magnitude. The subsequent training is conducted with observational data, including data augmentation by constructing several coadd fluxes from individual NB exposures. These are generated on-the-fly and weighted inversely by variance, including each exposure with a probability α , which is set here to $\alpha = 0.8$. This causes each galaxy to appear differently to the network in each epoch, i.e., each time the network parameters are adjusted, mimicking repeated measurements over the same sky areas and following systematic patterns to produce combined measurements with reduced noise, allowing the observation of fainter objects. This technique encompasses multiple issues when applied to observational data, such as variability in the number of exposures and the need to inform the network about which measurements are present.

Here, compared with Eriksen et al. (2020), we increase the number of layers in the autoencoder from ten to 20 while keeping the number of latent variables unchanged. Additionally, we adapted the input dimensions of the networks to fit the number of bands used. Specifically, in the W1 and W3 fields, the inputs comprise a maximum of 40 NBs and five BB from CFHTLenS, unlike the G09 field, where 40 NBs and nine BBs from KiDS and VIKING are used. Additionally, we studied the removal of eight blue NBs and the use of only NBs, as we outline in the Sect. 3.3.

Table 1. The first row gives the total sample size; the second row gives the size of the training sets; and the third and fourth rows give the size of the validation and test sets. The columns correspond to the fields. The samples resulting from the union of the training, validation, and test samples of W1 and W3 is presented in column 6, while the union of the samples of G09 and COSMOS is presented in the last column.

Samples	W1	W3	G09	COSMOS	W1+W3	G09+COSMOS
Total	30 065	12 234	4 313	11 890	42 299	16 203
Training	16 836	6 850	2 415	6 658	23 686	9 073
Validation	4 209	1 713	604	1 665	5 922	2 269
Test	9 020	3 671	1 294	3 567	12 691	4 861

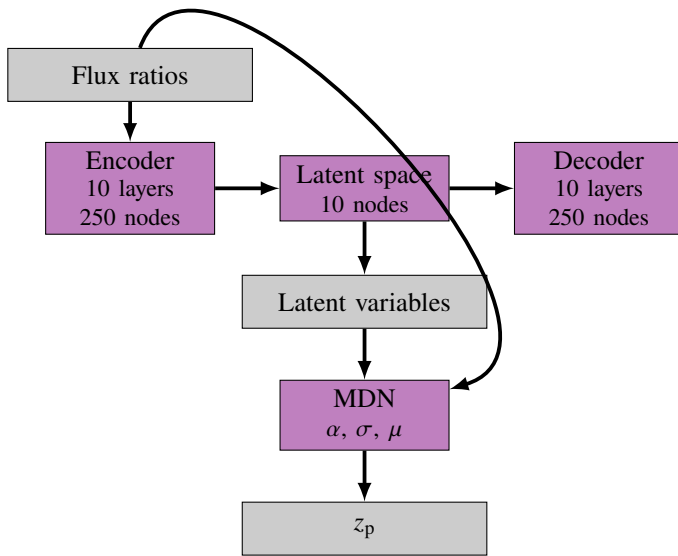


Fig. 2. DEEPz network flow diagram. The data are shown in grey and the networks in violet. The network architecture consists of an autoencoder with 10 layers and 250 nodes in both the encoder and decoder. Each layer includes linear transformations followed by ReLU non-linearities, batch normalization, and a 2% dropout, except for the last three layers. The autoencoder is fed galaxy flux ratios. The z_p network, which follows the same structure as the autoencoder, takes both the galaxy flux ratios and autoencoder features as input. It includes 1% dropout after all linear layers. This network is a MDN, representing the redshift distribution as a linear combination of 10 normaldistributions.

3.2. Metrics

To assess the precision of z_p , we have used the σ_{68} statistic as the primary metric (see Eq. 1). This statistic is calculated from Δz . Then

$$\sigma_{68} \equiv \frac{P[84] - P[16]}{2}, \quad (1)$$

where $P[x]$ represents the value of the Δz distribution at percentile x . σ_{68} is a centralised measure of the width or scatter in the accuracy of the estimated redshifts that is not affected by outliers.

We formally define *outliers* as galaxies that meet the condition

$$\frac{|z_p - z_s|}{1 + z_s} > 0.02. \quad (2)$$

Note that this equation is stricter than the outlier criteria typically used in BB papers (Hildebrandt et al. 2012).

3.3. Data refinement tests

During the reduction process and calibration, the collected observations undergo a series of steps and techniques aimed at improving their quality and completeness, eliminating possible errors in the measurements or defects such as noise or Galactic extinction, and extracting the most relevant information. These procedures involve curation and preprocessing techniques, along with the use of statistical tools such as univariate analysis for the selection of relevant features.

Here, seven tests were conducted to examine whether curation and preprocessing procedures, dependent on observational conditions and instruments, affect the precision of z_p . These tests ranged from combining measurements made by two instruments to selecting specific bands. Each test generated diverse datasets, which influenced the training of DEEPz and, consequently, the precision of the photometric redshifts.

Before describing the tests, we set out the baseline sample first

- *Baseline*: As a starting point for these studies, we exclude galaxies without a measurement in any of the BBs. Consequently, the samples of galaxies, both with and without spectroscopic information, are reduced by 9%, 11%, and 2% in the W1, W3, and G09 fields, respectively. These samples are used as a reference to evaluate and compare the performance of the tests.

Next we describe each of the tests performed.

- *Cross-validation (CV)*: The W1 and W3 fields have measurements classified as missing in the i -band of CFHTLenS due to issues with the filter identified as 'i.MP9702' during observation. However, new measurements were obtained using the successor filter, 'i.MP902', and part of the sample was completed with these values. Therefore, we evaluated the impact on the precision of the redshift by combining the measurements from these two filters, compared to the performance obtained without considering 'i.MP902' measurements, i.e., with the *baseline* sample. This is done to validate that there is no impact on z_p when using one of these two filters.
- *Infer missing NB values (non-NaN)*: The catalogue contains missing observations in some NBs. The DEEPz architecture uses a fixed number of inputs, making the code unable to handle a variable number of NBs. In Eriksen et al. (2020), the application of the code was restricted to galaxies with measurements in all 40 NBs. Imposing this condition results in the loss of 55.22% of the galaxies in the W1 field, around 38.52% in the W3 field, and 57.82% in the G09 field. To

reduce the impact on completeness, instead of removing all galaxies, we infer the missing NB values for galaxies with at least 30 NB measurements. In this case, the reduction in the sample size is 30% of the total sample of galaxies with at least one observation in the W1 field, approximately 28% in the W3 field, and 42% in the G09 field. The NB estimate was generated through a quadratic fit using the information from the g , r , and i -bands. This type of study allows us to estimate a more complete galaxy catalogue, including galaxies without observations in all filters.

- *Low Signal-to-Noise Ratio Fluxes (Low SNR)*: We investigate sources in the CFHTLenS catalogue that have at least one BB with a low signal-to-noise ratio, denoted by a value of 99. To generate a catalogue with a greater number of objects, we examine the impact of including sources under these conditions, even though this may not be the case for all bands, and catalogues are usually generated with high S/N based on the target band..
- *Bright Galaxies ($i_{AB} < 22.5$)*: We study if there is a significant difference in precision when faint galaxies are included or discarded in the analysis. Therefore, we cut the sample of galaxies at an apparent magnitudes of 22.5 according to the target band of the BB surveys corresponding to each wide field.
- *Galactic Extinction Correction (Ext. Correction)*: Although the wide fields used in this study are not at low Galactic latitudes, they are weakly and differentially affected by the dust, gas, and stellar density of the Milky Way, though the latter does not affect extinction. Therefore, we performed a correction to the NB and BB to undo the effects of Galactic extinction. Before the correction, we removed the Galactic extinction on the BBs of CFHTLenS based on the dust maps presented in Schlegel et al. (1998), which already included their apparent magnitudes, unlike the apparent magnitudes of the KiDS and VIKING surveys where they are not extinction corrected in our data. Subsequently, the correction was carried out for the BBs and NBs using the extinction values, $E(B - V)$, provided in the Planck 2015 thermal dust map (Aghanim et al. 2016). The Galactic extinction value at the source position and the corresponding correction factors were estimated through

$$\phi_{\text{corr}} = \phi_{\text{uncorr}} \cdot \frac{1}{C_0 \cdot E(B - V)^2 + C_1 \cdot E(B - V) + C_2}, \quad (3)$$

where the band-dependent coefficients (C_0 , C_1 , and C_2) were estimated using a second-degree polynomial fit to the median extinction affecting the Pickles stellar templates (Pickles 1998).

We conducted a univariate analysis of the bands and z_p using the Pearson correlation, mutual information, and regression methods (see Appendix A). We found that the BBs behave similarly in score to the NBs in terms of their importance for determining z_p according to wavelength and these methods, so it is interesting to study the case of only using the NBs to determine z_p . Additionally, we found a lower score for wavelengths in the blue, so we investigated their importance for the precision of z_p . The following two tests are based on this study.

- *Only NBs (NBs)*: We consider eliminating the BBs and using only the NBs. In this case, the NBs are normalised by creating an artificial band from the average of the NBs within the wavelength range of the target selection band, i.e., the i -band

in the case of fields W1 and W3 and the r -band in the case of field G09. This allows us to study whether the more general SED characteristics at low wavelength resolution and high SNR provided by the BBs are important in the precision of z_p . Therefore, as input, DEEPz uses the 40 NB fluxes normalized by the artificial band. This change in the number of bands used to determine z_p results in a change in the number of neurons in the input layer of the neural networks.

- *SED in the blue wavelength range (blue-lines)*: Since the univariate analysis shows a low correlation for wavelengths in the blue range of the galaxy SED, we explore the possibility of saving time by disregarding the detailed information about the SED in the blue wavelength range, contained in eight filters of the PAU survey, within the wavelength interval of 4550 Å to 5250 Å. Through this test, we evaluate the relevance of lines identified in the blue region with respect to the general SED characteristics within this spectral range when considering all wide bands.

In Table 2, we provide a brief description of each test and specify the number of galaxies in the training and validation sets for each case.

4. Results and Discussion

In Sect. 4.1, we perform a comprehensive analysis of the results obtained in each wide field and their combination. Additionally, we analyse the outcomes corresponding to the data refinement tests described in Sect. 3.3. In Sect. 4.2 we consider the origin of the spectroscopic redshifts and the effect on the z_p . Additionally, in Sect. 4.3 we compare our best results with the z_p obtained through the BCNz2 method. Finally, we describe the generation of the z_p catalogue in the wide fields in Sect. 4.4.

All measurements are performed in the intervals $18 \leq i_{AB} \leq 23$ and $z_s \leq 2$ unless stated otherwise.

4.1. Photometric redshift precision

In our study, the precision of the z_p is intrinsically linked to the field under consideration and the data available in each field. This is because the latter are used in the training process and validation, which depends on the fluxes of the NBs and BBs, the number of examples, and the distributions of z_s .

Therefore, in this section, we present the comparison of the results using the baseline samples of each field and their combinations. In Appendix B, the results of each data refinement test in each field and their combination are shown, implementing the training and validation samples differentiated by these conditions.

4.1.1. Performance by field

Initially, we consider each field individually, as well as the combination of the CFHTLenS fields, W1 with W3, and the KiDS /VIKING fields G09 with COSMOS. The analysis is carried out in terms of the σ_{68} trends, which are analysed in relation to the i -band magnitude limit and z_s .

We compare the precision of the baseline samples in the W1 and W3 fields and the combination W1+W3. We performed the same analysis for the baseline samples in the G09 and COSMOS fields and their combination. The behaviour of these two cases is shown in Fig. 3.

Data refinement tests	Description	Training Set		Validation Set	
Baseline	Galaxies without measurements in any of the bands are excluded.	W1+W3: 22 378	G09+COSMOS: 9 073	W1+W3: 5 581	G09+COSMOS: 2 269
Cross-validation (CV)	Comparison of <i>i</i> -band filters to confirm that the two CFHT filters provide consistent and comparable measurements.	W1+W3: 23 592	G09+COSMOS: 7 606	W1+W3: 5 581	G09+COSMOS: 1 902
Impute (non-NaN)	Investigation into handling galaxies with NaN values in the NB fluxes and the use of interpolation through p3.2cmp3.2cma quadratic fit.	W1+W3: 30 383	G09+COSMOS: 7 606	W1+W3: 7 561	G09+COSMOS: 1 902
Low signal-to-noise ratio fluxes (Low SNR)	Investigation of the treatment of low signal-to-noise ratio fluxes including those sources with magnitudes equal to 99.	W1+W3: 22 118	G09+COSMOS: 7 606	W1+W3: 5 529	G09+COSMOS: 1 902
Bright galaxies ($i < 22.5$)	We limit the magnitudes of the selected band to values less than 22.5.	W1+W3: 22 378	G09+COSMOS: 7 606	W1+W3: 5 581	G09+COSMOS: 1 902
Galactic extinction correction (Ext. Correction)	Study on the Galactic extinction correction in the BB and NB fluxes.	W1+W3: 22 378	G09+COSMOS: 7 606	W1+W3: 5 581	G09+COSMOS: 1 902
Only NBs (NBs)	Analysis of the importance of the more general features of the SED provided in the BBs.	W1+W3: 22 378	G09+COSMOS: 7 606	W1+W3: 5 581	G09+COSMOS: 1 902
SED in the blue wavelength range (blue-lines)	Indicates the importance of the lines detected in the blue range.	W1+W3: 22 378	G09+COSMOS: 7 606	W1+W3: 5 581	G09+COSMOS: 1 902

Table 2. Summary of studies on observational effects in photometric redshift estimation. Dimensions of the training and validation sets for the combination of data in W1 and W3, and for the combination of data in the fields G09 and COSMOS.

As expected, in all fields, it can be seen that the precision in terms of σ_{68} , as a function of i and z_s , is higher for bright and nearby galaxies (lower σ_{68}), and decreases for faint and distant galaxies (higher σ_{68}). When comparing the values obtained from each test in each individual field, we find a systematic superiority in the precision of W1 over W3 and of G09 over COSMOS. We also find that the combination of fields with the same NBs and BBs, W1+W3 and G09+COSMOS, produces better results than the individual samples W3 and COSMOS, respectively, in terms of the σ_{68} trends when studied as a function of i and z_s , compared to using individual samples from each field. Regarding the comparison of results between the W1+W3 and G09+COSMOS samples, differentiated by the photometry and spectroscopic redshift catalogues, we observe that in all studies, W1+W3 outperforms G09+COSMOS. The G09 and COSMOS fields have four more BBs than the CFHTLenS fields but with lower SNR; this does not generate differences in the trends of the metrics measured as a function of i and z_s between G09+COSMOS and the CFHTLenS fields. However, we note that DEEPz determines z_p with less precision in G09+COSMOS compared to W1+W3 as in the individual comparisons.

4.1.2. Analysis of the data refinement tests

The comparison between refinement tests is shown in Fig. 4, in which we show the trends of σ_{68} and the fraction of outliers as a function of apparent magnitudes in the *i*-band, z_p , and z_s for sets of models trained with different galaxy samples. Two baseline

samples are taken, one combining galaxies from the W1 and W3 fields of CFHTLenS and the other galaxies from the G09 and COSMOS fields of KiDS plus VIKING. These two samples are adapted to the specific conditions of each test, and each model is trained with them. The trends are obtained with the baseline samples, i.e., without any restriction.

We now comment on the test in the same orders as they were presented in Sect. 3.3:

- *CV*: The CV test revealed that galaxies in the W1, W3 fields, and their combination, do not show a degradation in the precision of z_p when including measurements from different filters with similar sensitivities in the *i*-band of the CFHTLenS catalogue. Therefore, the differences between the measurements from two filters are not statistically significant. Consequently, we can obtain more comprehensive catalogues, such that the measurements of both instruments are indistinguishable within the precision limits of the zero point.
- *Infer missing NBs*: Inferring missing data in the NBs increases the sample size by approximately 35% in W1 and W3, and around 20% in G09 and COSMOS. The results suggest that inferring missing data in this way is an effective strategy for improving catalogue completeness without significantly affecting the performance of redshift determination. In fact, this is the test that shows the best performance in both W1+W3 and G09+COSMOS.
- *Low SNR*: It can be seen that sample loss due to low signal-to-noise ratio in the BBs is not significant in any field, accounting

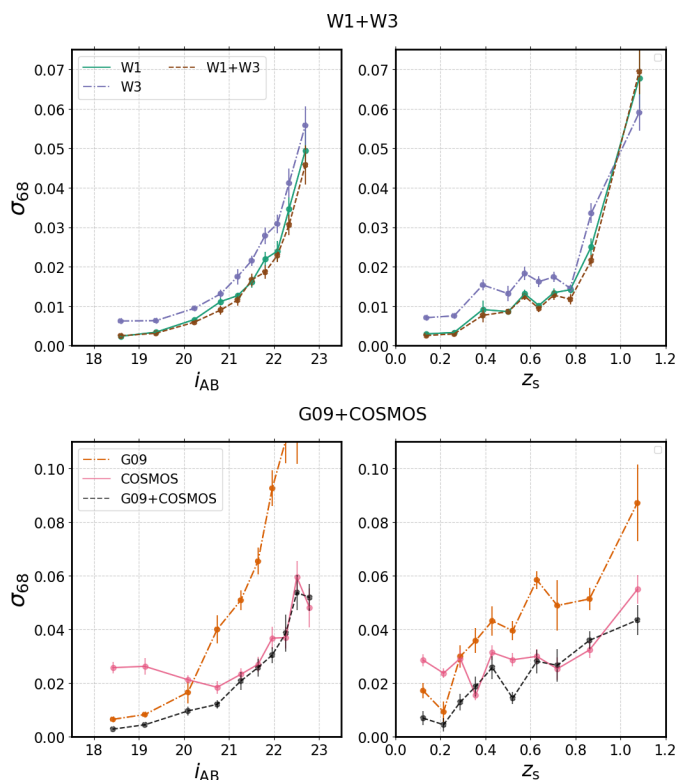


Fig. 3. Trends in the measurement of σ_{68} . The distribution is divided into ten bins, each containing the same number of objects, based on the apparent magnitude in the i -band and z_s , in the left and right columns, respectively. These trends show the precision, in terms of the centralised scatter σ_{68} , in the W1+W3 and G09+COSMOS validation sets.

for around 1% of the sample. Therefore, the performance in these samples is very similar to that obtained with the baseline samples.

- $i < 22.5$: The analysis of galaxies limited to apparent magnitudes brighter than $i_{AB} < 22.5$ indicates good precision, as in the other tests, but shows a decrease in precision for a sample of galaxies that include magnitudes close to 23 and at high redshifts, compared to the other data refinement tests. This slight decrease in precision is a little more noticeable in the G09 and fields.
- *Ext. Correction*: We find that the Galactic latitude of the fields does not have any effect on the precision of z_p provided that the extinction correction in Eqn. 3 is applied.
- *NBs*: In the analysis focused on using only the NB in the photometric redshift estimation, in the W1+W3 sample, a reduction in precision is observed with increasing i -band magnitude and redshift, and this more pronounced than in other tests. However, the model performance remains similar to the other cases at low redshifts and for bright galaxies. This suggests that for these two fields, ignoring the BB does not significantly affect the precision in z_p for galaxies with $i < 20$, as there is a high SNR in the NBs. For the G09+COSMOS sample, we find poor performance for both faint and bright galaxies, as well as for close and distant galaxies. This finding underlines the importance of the number of examples with which the network is trained, since the training sample in this field is smaller than that for W1+W3, and the NB fluxes have the same SNR.
- *Blue-lines*: The performance of DEEPz does not show any significant changes when the detailed SED features provided

by NBs in the blue wavelength range are omitted, so they may not be necessary to estimate z_p in the W1, G09 and W3 fields.

Since the model trained with the full NB sample has the best performance compared to other tests in W1+W3 and G09+COSMOS, we have decided to adopt this methodology as the main one for determining the photometric redshift. That is, the model will receive as input galaxies with information from 40 NBs + BBs, with the number of the latter depending on the field. In the event that a galaxy has at least ten missing measurements in NBs, a quadratic fit on BBs will be made to infer these measurements.

To improve the completeness of the photometric redshift catalogues, we include the methodology of models trained with galaxies with imputation in the i -band of the CFHTLenS catalogue, i.e., the CV samples and the models trained with galaxies with low SNR. Since these two models show a similar precision to that obtained with the baseline model in the trends of σ_{68} and the outlier fraction for weak and distant galaxies in each field or their combination.

4.2. Effect of spectroscopic surveys

When spectroscopic catalogues present non-uniform distributions in z_s , contain sources of variable brightness, data affected by contamination by absorption lines or exposure time limitations, the recovered z_p will reflect these conditions. Therefore, in our analysis, we also consider the origin of the redshifts in the study, since in each field at least the combination of two spectroscopic catalogues is used, and the ranges and statistics of the distributions of z_s of these differ, as illustrated in the upper panel of Fig. 5. We compare the dominant redshift distributions of the baseline sample in the W1 field, VIPERS and GAMA_SDSS. The upper panels show the trends of σ_{68} with respect to i and z_s , respectively.

The performance comparison between the VIPERS and GAMA_SDSS samples was carried out with the same number of sources from the baseline sample in the W1 field, taking the largest possible number of examples from each survey, resulting in samples of 1760 galaxies.

The σ_{68} trends in the W1 area, separated by the VIPERS and GAMA_SDSS samples, show slight differences for faint and distant galaxies. VIPERS has higher precision than GAMA_SDSS. Although both surveys include measurements for this type of galaxy and were used in the model training, the number of examples from each survey is different in these ranges.

Finding this dependency in the spectroscopic survey data indicates that there will be better precision in the photometric redshifts for galaxies with the characteristics of the survey with the majority of examples.

4.3. Comparison between DEEPz and BCNz2

We present the z_p of the W1 and G09 baseline test samples obtained with models trained with W1+W3 and G09+COSMOS samples, respectively, along with z_p obtained in Navarro-Gironés et al. (2023), which use the method BCNz2.

In Fig. 6, we show the trends of σ_{68} and the fraction of outliers with respect to the apparent magnitude in the i -band and the spectroscopic redshift obtained with BCNz2 and DEEPz for the W1 and G09 baseline samples.

The measurements of z_p in the W1 and W3 fields indicate that the σ_{68} metric, for both DEEPz and BCNz2, shows the expected behaviour: a decrease in precision and an increase in

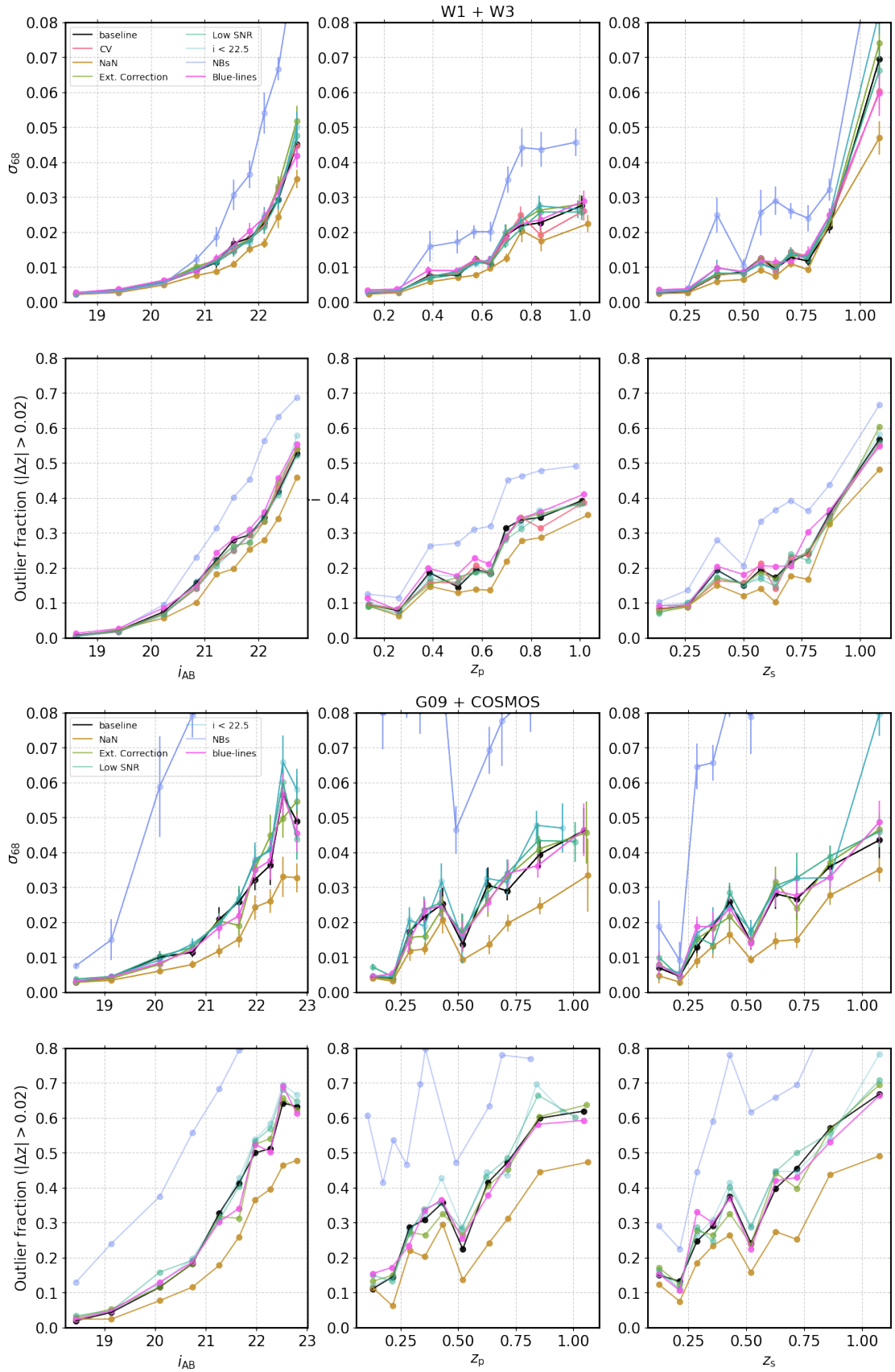


Fig. 4. The upper row depicts trends and variations in the measurement of σ_{68} , while the lower row shows the fraction of outlier values. The distribution is divided into ten bins, each containing an equal number of objects, based on the magnitude in the i band, z_p , and z_s , positioned in the left, centre, and right columns, respectively. These trends represent the findings from seven tests, summarised in Table 2, implemented on the W1+W3 and G09+COSMOS baseline samples.

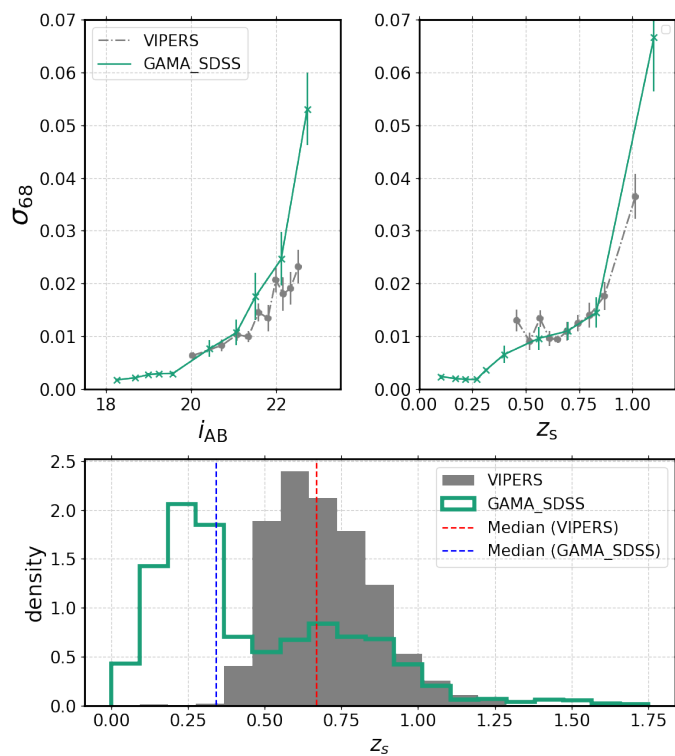


Fig. 5. The upper panels show trends in the measurement of σ_{68} with respect to i (left panel and z_s , right panel). There are separate curves for the results using the the VIPERS and GAMA_SDSS redshifts. The lower panel shows the spectroscopic redshift distribution from the VIPERS and GAMA_SDSS surveys in the W1 field.

the fraction of outliers moving to fainter galaxies and higher spectroscopic redshifts. The performance of the two methods is similar for bright galaxies up to an apparent i -band magnitude of approximately 20 and for nearby galaxies up to a redshift of around 0.3. However, beyond these values, DEEPz is more accurate than the template method BCNz2, reaching a difference in σ_{68} of $0.02(1+z_s)$ between the two methods for faint galaxies with an apparent magnitude in the i -band of 23.

This observed trend between DEEPz and BCNz2 on the W1 baseline sample using the model resulting from the combination of the W1 and W3 fields is consistent with that found in the individual studies of the W1 and W3 fields, for any data refinement test. It is also consistent with the measurements in the COSMOS field, where the methods are applied to samples with a range of apparent magnitude limits in the i -band in [20 - 22.5]. However, this behaviour is completely different in the case of bright galaxies in the i -band, i.e., for the G09 baseline sample, the BCNz2 template method is more accurate than DEEPz in all cases. However, when a model is implemented with the combination of galaxies from the G09 and COSMOS samples on the G09 baseline sample, DEEPz shows an improvement in precision for bright galaxies but not larger than that for BCNz2. These results show that the precision of DEEPz increases as the number of examples in the training sample increases, as well as when the number of BB filters increases, as demonstrated in the COSMOS field (Eriksen et al. 2020).

Since we have an estimate of the error behaviour of each method according to i and z_s , we wonder if there is any correlation in the errors of each method, i.e., if the two methods tend to underestimate or overestimate the redshift in the same way. Fig. 7 shows the comparison of errors Δz from each method,

categorised by apparent magnitude in the i -band and z_s using a colour code. For the baseline sample, we find that the two methods tend towards the perfect case, i.e., if both methods determined z_p identical to z_s , all points would be concentrated at a single point in the centre of the plot. In the scatter plots, we see that the errors of DEEPz and BCNz2 correlate linearly, meaning that there is a set of galaxies for which both methods determine z_p with the same level of precision. This is to be expected as both methods use the same photometry. Additionally, on the scatter plots, we observe two patterns, one horizontal and one vertical, located at zero on each axis. These patterns indicate that there are cases where one method is more accurate than the other. However, we find less dispersion overall for the DEEPz method. Additionally, we observe that both methods decrease in precision when the apparent magnitude in the i -band and the redshift z_s increase.

4.4. Catalogues

Based on the results obtained in each field and the study regarding observational effects, as well as the performance comparison between DEEPz and the BCNz2 template method presented in Navarro-Gironés et al. (2023), we have generated catalogues of photometric redshifts in the W1, W3, and G09 fields. In all three fields, we have chosen to utilise the non-NaN model, which uses a training set with inferred values for missing NBs obtained using a fit to the measurements in the r , g and i -bands.

We applied the CV and Low SNR models as additional strategies to enhance the completeness of the catalogues. In the first case, we combined the galaxies belonging to W1 and W3 that have measurements with the second filter in the i -band and galaxies with low SNR in both the W1 and W3 fields. The resulting z_p catalogue in the W1 field has 388 375 galaxies, of which 86 were assigned a $z_p = 0$, which means the model could not determine a value. After excluding these, a total of 388 289 galaxies had a photometric redshift estimated with a mean $z_p = 0.59$. In the W3 field, 779 935 photometric redshifts were obtained with an average $z_p = 0.58$, excluding 172 galaxies with $z_p = 0$. Lastly, in the G09 field, the photometric redshifts of 490 617 galaxies were estimated, with an average $z_p = 0.60$, after discarding 31 galaxies with $z_p = 0$.

5. Close galaxy pairs

To study the performance of z_p obtained here in a specific application, the identification of close galaxy pairs are analysed. From the study of the interaction between the members of these systems, it can be inferred how their physical properties are affected (Toomre & Toomre 1972; Mesa et al. 2014). The identification of pairs of close galaxies in the W1 and W3 fields and the estimation of their properties are carried out following the methodology described in Gonzalez et al. (2023). We compare our results to those obtained in the same study, where the photometric redshifts were determined using the BCNz2 method.

Gonzalez et al. (2023) analyse two samples, one considering the entire galaxy catalogue in each field (*total sample*) and the other after applying a quality cut using the photometric redshift values obtained with BCNz2 (*gold sample*). Here, the comparison of the performance of z_p in the identification of pairs of galaxies is performed on the *total sample*. This sample matches 99.65% of our catalogue with the BCNz2 sample in the W1 field and 97.05% of the BCNz2 sample in the W3 field.

The identification of pairs of galaxies is carried out using the algorithm described in Rodriguez et al. (2020), which applies criteria regarding the projected distance between galaxies ($r_p < 50$

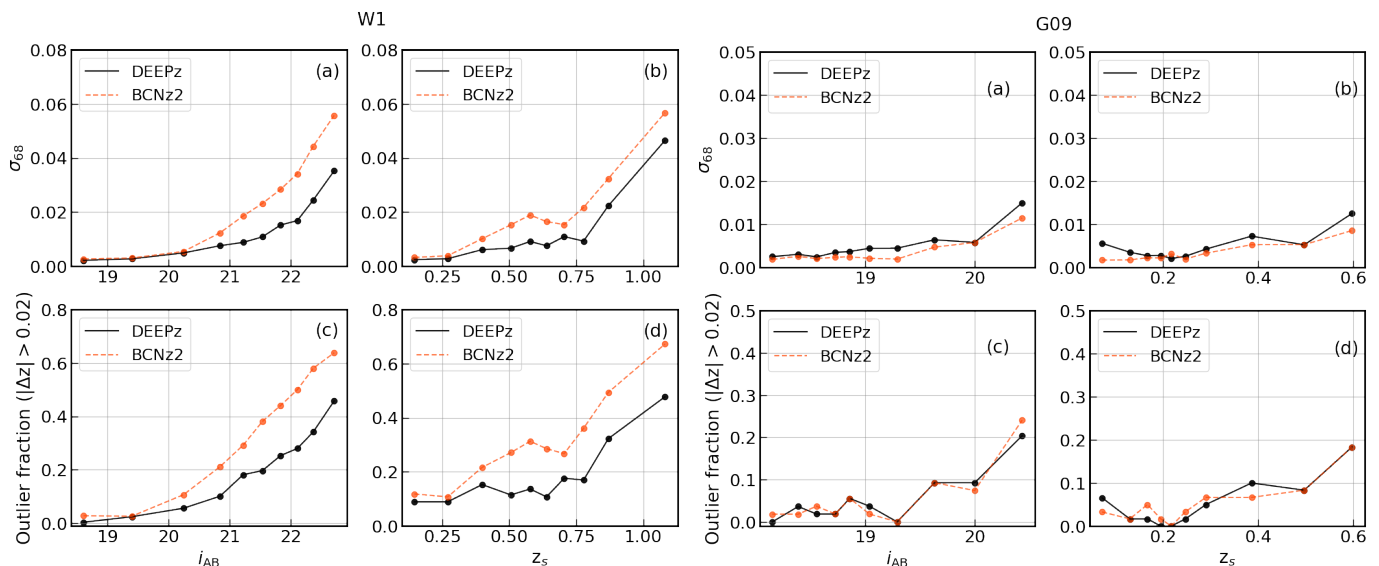


Fig. 6. Comparison of the σ_{68} values (top row) and outlier fractions (bottom row) for the W1 and G09 baseline samples obtained using the DEEPz and BCNz2 methods. Columns (1) and (2) correspond to the implementation of the model trained with the W1 sample with missing NB values inferred. Columns (3) and (4) correspond to the implementation of the model trained with the G09+COSMOS sample with missing NBs fluxes inferred. Upper panels (a) and (b): σ_{68} for DEEPz and BCNz2 plotted against i -band magnitude for (a) and redshift for (b). Lower panels (c) and (d): Fraction of outliers with $|\Delta z| > 0.02$ plotted as a function of i -band magnitude for (c) and redshift for (d).

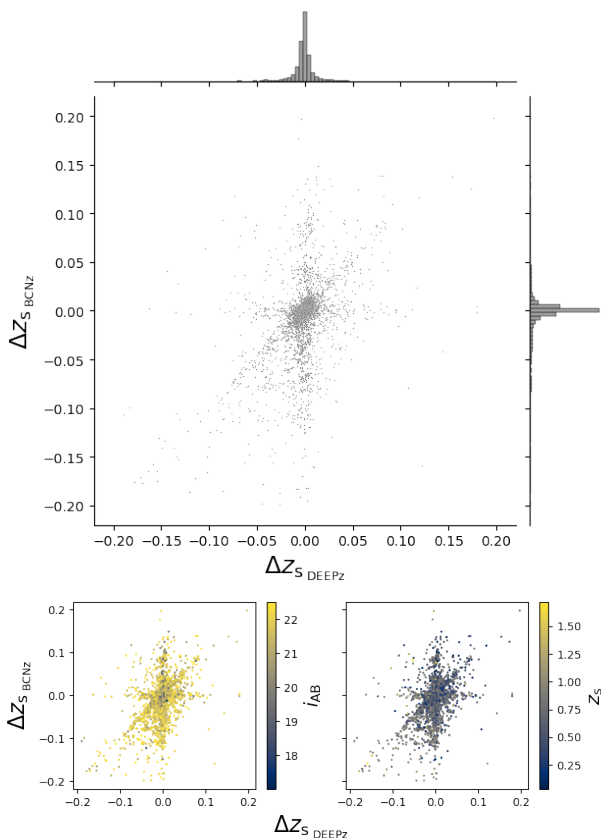


Fig. 7. Scatter plots of errors on the x-axis for the DEEPz method and on the y-axis for the errors obtained when determining z_p using the BCNz2 method. *Top panel:* Scatter plot of errors for each method along with a histogram showing the distribution of points along each axis. *Bottom left panel:* Scatter plot of errors for each method colour coded according to the apparent magnitude in the i band. *Bottom right panel:* Scatter plot of errors for each method colour coded according to z_s .

Sub-sample	DEEPz	BCNz2
all pairs	2,157	2,282
$M_r^p < -22.5$	320	338
$M_r^p \geq -22.5$	1,837	1,944
$z_p < 0.4$	835	852
$z_p \geq 0.4$	1,322	1,430
$L_2/L_1 < 0.5$	1,221	1,251
$L_2/L_1 \geq 0.5$	936	1,031
blue pairs	1,063	1,103
red pairs	1,094	1,179

Table 3. Number of close galaxy pairs resulting from the identification with DEEPz or BCNz2 in total samples and the subsample, selected according to their absolute magnitude in the r -band (M_r), the pair redshift (z_{pair}), the luminosity ratio between the satellite and primary galaxy (L_2/L_1), and the colour.

kpc), the difference in projected velocity ($\Delta V < 3500$ km/s), and isolation. Despite the difference in the number of galaxies used to generate pairs, the number of pairs of galaxies identified is similar in both fields. In the W1 field, 656 pairs were detected through z_p determined by DEEPz (z_{DEEPz}) and 637 pairs with z_p from BCNz2 (z_{BCNz2}). In the W3 field, 1 521 pairs were found with z_{DEEPz} and 1,627 pairs with z_{BCNz2} . Additionally, as shown in Table 3, we also find that the number of galaxy pairs obtained using both catalogues agree in the different samples defined according to the absolute magnitudes in the r -band of the pairs, defined as $M_r^p = -2.5 \log(L_1 + L_2)$, where L_2 and L_1 represent the luminosities in the r -band of the fainter and brighter galaxies in the pair system, respectively. We also found similarity in the luminosity ratio between the members of the pairs (L_2/L_1), the redshift of the pair, and the classification of the pairs according to the colour-magnitude diagram into red and blue categories, as set out in Gonzalez et al. (2023).

Among the estimated properties, the mass was determined using weak gravitational lensing stacking techniques in the subsets already defined (see Table 3). Through stacking techniques,

the signal-to-noise measurement of the lensing effect is improved by artificially increasing the source galaxy density, from which the lens parameters are derived. This allows the calculation of the posterior probability distribution, which in this case refers to the probability distribution of the mass of the galaxy pair. It is obtained by considering Bayesian techniques, where prior information about the parameters (the prior distribution) is combined with the information provided by the data (the likelihood) to obtain the posterior distribution. The posterior density distributions were analysed, considering the physical properties described in Table 3. Additionally, the analysis includes the results obtained in Gonzalez et al. (2023) through the BCNz2 method on the *total sample*.

As seen in Fig. 8, the posterior density distributions for the DEEPz and BCNz2 methods are shown for the samples based on magnitude, colour, redshift, and luminosity ratio criteria. For samples selected under magnitude and colour criteria, we found similar trends and values. The probability profiles for pairs with $z < 0.4$ and red pairs show differences, such that the pairs identified with DEEPz that are close and red are less massive compared to BCNz2. For pairs with $z \geq 0.4$ and satellite galaxies that meet $L_2/L_1 \geq 0.5$, we found that DEEPz pairs are more massive compared to BCNz2. Nevertheless, the error intervals of the medians of all distributions overlap. Consequently, the mass estimates for both samples are statistically equivalent.

While the samples of DEEPz and BCNz2 pairs are compatible in terms of number and mass, even when selecting subsamples, we find that only 249 are common pairs, meaning the central and satellite galaxies of the pair coincide. This amount represents approximately 40% of the total number of pairs obtained with z_{DEEPz} .

Regarding complementary galaxy pairs, which are pairs that do not match in the identifications made through z_{DEEPz} and z_{BCNz2} , we find that 250 galaxy members are present in both catalogues. Of these 250 galaxies, it was observed that central galaxies in DEEPz are identified as satellites in BCNz2 in three cases, and vice versa, satellite galaxies in DEEPz are classified as central in BCNz2 in three instances. Despite having the same number, they are not related as pairs; in other words, the central galaxy in one catalogue does not become a satellite in the other. Therefore, the similarity in number and properties results from the identification algorithm, which links close galaxies that are likely in the same environment, implying that they have similar physical properties and also inherit the global properties of the sample used for their identification.

When comparing the distributions of photometric redshifts of the pairs, represented in Figure 9 through histograms and box plots¹, we observe that the common pairs identified with z_{DEEPz} and z_{BCNz2} ($z_{\text{DEEPz}}^{\text{com}}$ and $z_{\text{BCNz2}}^{\text{com}}$) tend to have lower val-

¹ In the boxplot diagrams, the top and bottom lines of the boxes represent the 25th and 75th percentiles of the distributions, while the wrists of the boxes represent the medians. Notches display the confidence interval (95% confidence level) symmetrically around the medians. When comparing distributions, if the notches of two boxes do not overlap, there is a statistically significant difference between the medians (McGill, Tukey, & Larsen 1978; Krzywinski & Altman 2014). For skewed distributions or small sized samples it might be the case that the CI is wider than the 25th or 75th percentile, therefore the plot will display some “inside out” shape. The lines extending from the boxes are called whiskers. The boundary of the whiskers is based on the 1.5 interquartile range (IQR) value. The whiskers extend from the bottom/top of the boxes up to the lowest/largest data point that falls within 1.5 times the IQR. The whisker lengths might not be symmetrical since they must end at an observed data point.

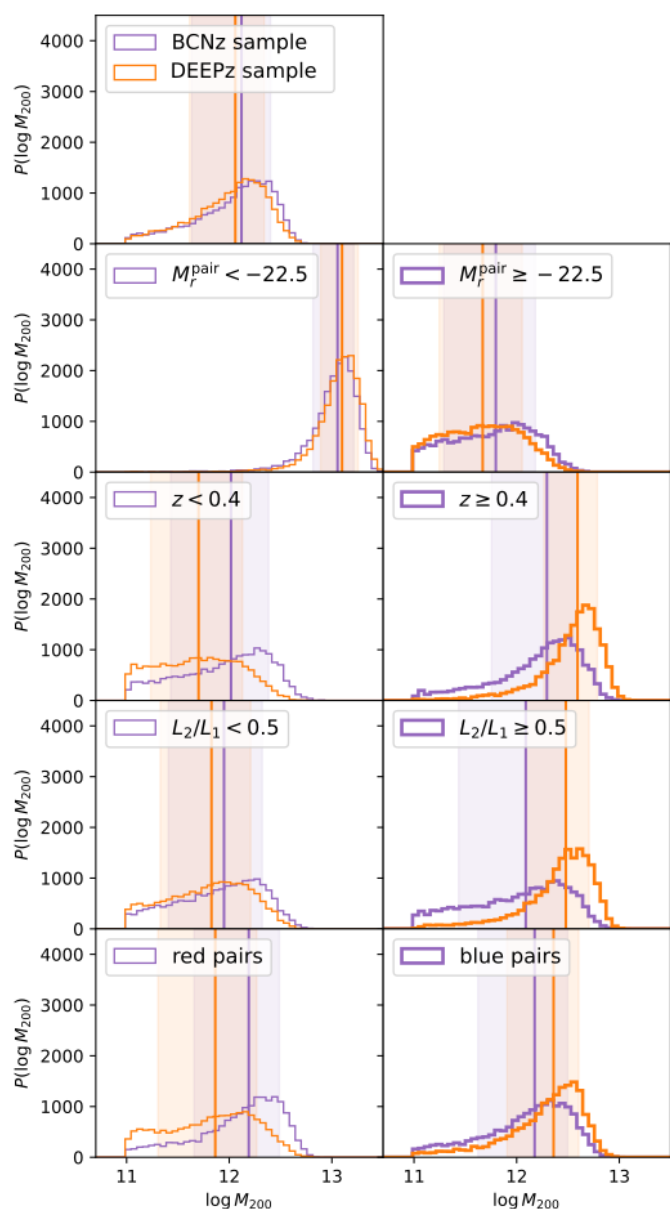


Fig. 8. Posterior density distributions of the fitted $\log M_{200}$. Each row shows the distributions for the pairs selected from the BCNz2 and DEEPz methods in purple and orange, respectively. The selection cuts according to pair properties are shown using thicker and narrower lines as referred to in the legends. Vertical lines indicate the median values and the shaded regions enclose 68 per cent of the distributions corresponding to the errors. In each panel, the stacked pair sub sample described in Table 3 is specified.

ues compared to their complementary sets ($z_{\text{DEEPz}}^{\#}$ and $z_{\text{BCNz2}}^{\#}$). This difference is significant, as the confidence intervals of the box plots do not overlap, indicating that the medians of z_p of $z_{\text{DEEPz}}^{\text{com}}$ and $z_{\text{BCNz2}}^{\text{com}}$ are statistically different from their complements. However, the statistical difference in the medians of z_p between common pairs and their complements is likely because the redshifts of the latter are higher due to the increased volume. This is evident as their z_p distribution extends across the entire range.

This behaviour is in agreement with what was observed in the comparison between σ_{68} and the fraction of outliers with respect to the apparent magnitude in the *i*-band and z_s bands for both

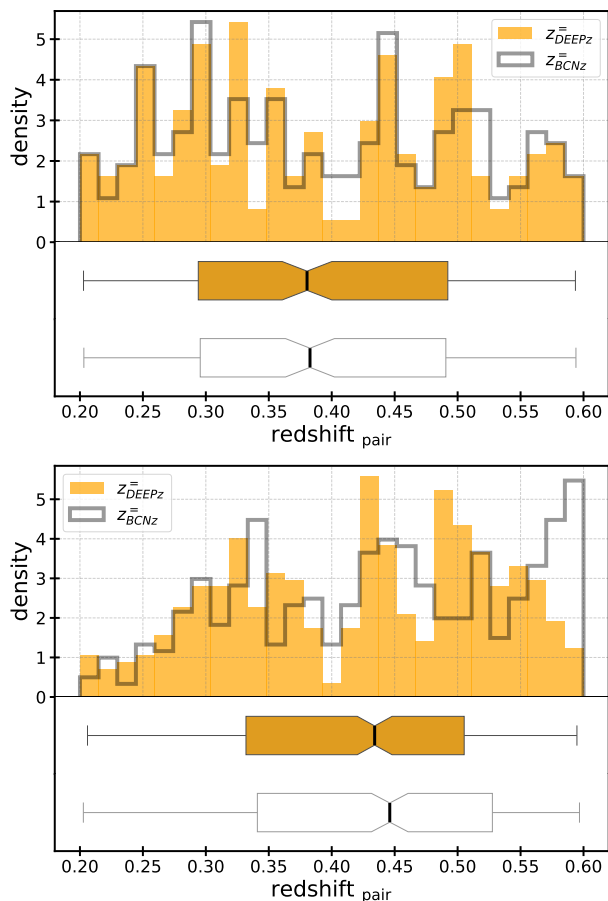


Fig. 9. Histograms and box plots are used to compare the distributions of the photometric redshifts of close galaxy pairs. Orange represents the sub samples of pairs determined using z_{DEEPz} , and black represents sub samples of pairs determined with z_{BCNz2} , respectively. *Upper panel:* distributions correspond to the samples: DEEPz^{\cap} , BCNz2^{\cap} . *Lower panel:* distributions correspond to the samples: DEEPz^{\neq} , and BCNz2^{\neq} .

methods. The redshifts determined by each method for bright, close galaxies are similar in their trends and precision. Regarding galaxies with apparent magnitude in the i -band fainter than 20 and z_{pair} greater than 0.3, the σ_{68} measurements between these two methods show differences of up to ~ 0.02 in the estimates of z_p for the faintest galaxies with respect to the apparent magnitude in the i -band, with DEEPz showing higher precision compared to BCNz2. Additionally, we find from galaxies with spectroscopic information that the difference between the pairs of each method is due to when one of these methods deviates significantly from the actual redshift value of the member galaxy of the pair, as shown in Fig. 10. Where we observe that the larger the errors in one of the member galaxies of the pair, the more likely the difference between pairs identified with the z_p of DEEPz and BCNz2.

Considering the behaviour between the two methods and the fact that the only difference in identifying close galaxy pairs is the determination of the photometric redshift, it is estimated that DEEPz agrees with the purity and completeness ranges of close galaxy pair catalogues, as described in Table 1 of (Rodríguez et al. 2020), under the criteria of magnitude $i < 22.5$ and spectroscopic redshift $0.2 < z < 0.6$.

Therefore, we can initially conclude that the photometric redshift catalogues generated with DEEPz are effective for the identification of galaxy pairs. Furthermore, through the identification

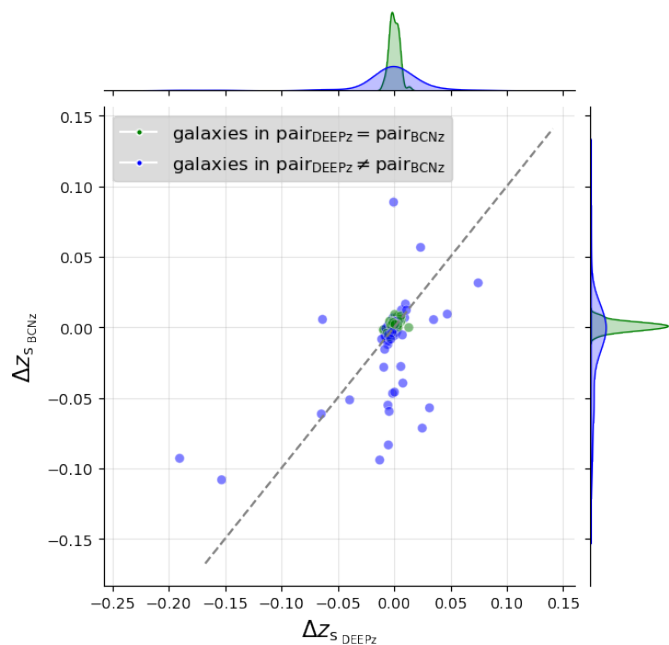


Fig. 10. Scatter plot between the errors of DEEPz and BCNz2 along with the density distributions of galaxies in common pairs ($\text{pair}_{\text{DEEPz}} = \text{pair}_{\text{BCNz2}}$) and galaxies in non common pairs ($\text{pair}_{\text{DEEPz}} \neq \text{pair}_{\text{BCNz2}}$) between the two methods.

of common pairs and their complements, along with the Δz values of the member galaxies obtained with each method, we observe that combining both methodologies can increase the purity of pair catalogues when the same pairs are identified, and also test their performance. However, a more detailed study is needed to correlate the photometric errors of each method with the identification of galaxy pairs and their properties.

6. Conclusions

PAUS is an optical survey made using the PAUCam instrument on the William Herschel Telescope in La Palma, Canary Islands. The survey employs 40 narrow-band optical filters evenly spaced at 100 \AA intervals, covering a range from 4500 \AA to 8500 \AA , and achieving an average spectral resolution of $R \sim 65$. Focusing on fields such as COSMOS, CFHTLS (W1, W3, W4), and KiDS/GAMA G09, PAUS has covered substantial sky areas: 12.04 deg^2 in W1, 15.7 deg^2 in G09, 22.64 deg^2 in W3, and 1 deg^2 in COSMOS. This extensive coverage supports large-scale cosmological studies and research on galaxy evolution. We present the estimation of the photometric redshift of galaxies in three of the fields observed by PAUS: W1, W3, and G09. Our analysis includes studies aimed at improving the precision and completeness of the galaxy catalogue by addressing various aspects of the observations and their processing. We compare our DEEPz photometric redshift measurements with those presented in Navarro-Gironés et al. (2023) using the BCNz2 template method. We implement our photometric redshifts in the identification of close galaxy pairs as a test case.

For the estimation of z_p in each field, a combined approach using simulated and observational data was employed. The observational data included information from individual exposures, combined fluxes from 40 narrow bands (NBs) of PAUS, broad-band (BB) data from CFHTLenS in the W1 and W3 fields, and

KiDS + VIKING in the G09 field, in addition to spectroscopic redshifts from various studies.

The methodology utilised DEEPz (Eriksen et al. 2020) as the main tool, a code tested in the COSMOS field that includes three neural networks: two autoencoders and a mixture density network. It implements transfer learning, meaning the networks are pretrained with simulated data before being trained with observational data. The training process involves data augmentation by creating co-additions of individual exposures of observations in the 40 NBs. The architecture of the networks is adjusted according to the field or study, analysing the importance of different sets of photometric data to improve the precision of z_p . The primary metric used to evaluate the precision of photometric redshifts was the centralised scatter, σ_{68} (see Eq. 1), derived from the distribution of relative differences between spectroscopic and photometric redshifts. Additionally, the fraction of outliers with $|\Delta z| > 0.02$ (see Eq. 2) was used as a secondary metric.

First, we studied the performance of DEEPz when the models were built using samples from the individual fields: W1, W3, G09, and COSMOS, as well as combinations of W1+W3 and G09+COSMOS. Then, seven tests were conducted regarding data refinement to assess their impact, if any, on the precision of z_p . Each test generated various datasets that influenced the training of DEEPz and, consequently, the precision of the photometric redshift. More specifically, the tests addressed:

Cross-validation (CV): The impact on redshift precision was evaluated by combining measurements from two different filters ('i.MP9702' and 'i.MP902') of the i -band from CFHTLenS. The aim was to validate that there is no significant impact on z_p when using either of these two filters.

Impute (non-NaN): To address missing observations in some narrow bands (NBs), missing values were imputed using a quadratic fit based on the g , r , and i bands. This procedure reduced data loss and allowed the inclusion of galaxies without observations in all NBs, improving the completeness of the galaxy catalogue.

Low Signal-to-Noise Ratio Fluxes (Low SNR): The impact of including sources with at least one broadband (BB) with a low signal-to-noise ratio, classified with a value of 99, was investigated. This allowed generating a catalogue with a larger number of objects.

Bright Galaxies ($i < 22.5$): The difference in precision was studied by including or excluding faint galaxies. The sample was limited to galaxies with apparent magnitudes less than 22.5 in the target BB of each wide field study.

Galactic Extinction Correction (Ext. Correction): Galactic extinction in the fluxes of NBs and BBs was corrected using Planck Collaboration (2016) (Aghanim et al. 2016) dust maps. This correction was made to account for the effects of differential extinction caused by dust, gas, and stellar density of the Milky Way.

Only NBs (NBs): The utility of using only NBs by eliminating the BBs was investigated. The NBs were normalised by creating an artificial band from the average of the NBs within the wavelength range of the target selection band. This approach allowed studying the importance of more general SED features in the precision of z_p .

SED in the blue wavelength range (blue-lines): The possibility of saving time by discarding detailed SED information in the blue wavelength range (4550 to 5250 Å) was explored, based on a univariate analysis showing low correlation in this range. The relevance of the lines identified in the blue region was evaluated concerning the general SED features in all broadband.

Additionally, we studied if there is any dependence on the photometric redshift precision based on the spectroscopic samples used in the training of DEEPz.

We found that the precision of the photometric redshift determined with DEEPz in the wide fields and their combinations is less than $\sigma_{68} = 0.06$ compared to the baseline samples of W1+W3 and G09+COSMOS, which reach apparent magnitudes in the i -band of 23 and 22.5, respectively. This behaviour holds, except for the model trained solely with a sample from G09 with $i_{AB} < 20$. However, as expected, in all studies, we observed an increase in the number of outliers as galaxies become fainter and their redshifts grow.

The combination of the W1 with W3 fields and G09 with COSMOS fields produces better results in terms of precision trends (reduced σ_{68}) and lower outlier fraction with respect to the apparent magnitude in the i -band and z_s , compared to using individual field samples. Regarding the comparison between fields with the same photometric information, there is a systematic predominance of W1 over W3 and G09 over COSMOS. The former is due to differences in sample size, and the latter is attributed to the G09 datasets having spectroscopic information that only considers bright galaxies. Regarding the comparisons between combinations, the W1+W3 combination tends to slightly outperform G09+COSMOS.

Based on the refinement tests and the analysis of the effect of observational samples on the precision of z_p , we can draw some conclusions:

Instrumental: Concerning the instrumental refinement tests, the CV study revealed that galaxies in the W1, W3 fields, and their combination, W1 combined with W3, do not show a degradation in the precision of z_p when including data from different filters with similar sensitivities in the i -band. This also holds true when galaxies are lost due to a low signal-to-noise ratio, as these measurements in each field represent approximately 1% of the samples.

Properties: In the analysis focused solely on NB, a reduction in precision was found with increasing magnitudes in the i -band and redshifts compared to other studies. However, the model performance remained similar in terms of low redshifts and bright galaxies. This trend suggests that for these specific galaxies, excluding broad bands does not significantly affect the precision of z_p . This finding highlights the importance of the general SED characteristics provided by broad bands in determining photometric redshifts using the DEEPz method. The results obtained without NBs in the blue wavelength range showed similarities with the low signal-to-noise ratio study, indicating that the detailed characteristics in the SED provided by NBs in the blue wavelength range may not be necessary to estimate z_p in the W1, W3, and G09 fields.

Completeness: The inclusion of inferred NB data (non-NaN) increased the sample size by approximately 35% in W1 and W3 and around 20% in G09 and COSMOS. It also proved optimal for improving the performance of DEEPz compared to the other tests. This suggests that filling in the missing NB values is an effective strategy for generating photometric redshift catalogues with good precision. In G09+COSMOS, this study also shows a superior performance trend compared to other models. However, due to sample sizes, the measurements fall within confidence intervals, implying that the medians in each bin of magnitude and redshift are not statistically different. Despite this, we have consider this approach the best strategy for generating z_p catalogues in any of the fields.

Spectral Biases: We found a dependence of z_p precision on the spectroscopic survey used in the training. This gives us an implicit

measure that there will be better photometric redshift precision for galaxies with the characteristics of the survey predominant in the number of examples, in our case, VIPERS.

Regarding the comparison between the DEEPz method and the template method BCNz2, we found similar trends in accuracy for both apparent magnitude in the i -band and z_s . However, DEEPz demonstrates a 20 to 50 per cent reduction in σ_{68} and outlier fraction for the faintest galaxies ($i = 21 - 23$) compared to BCNz2 (see Fig. 6). We also observed a linear correlation between their errors, with both methods slightly tending to underestimate errors within certain redshift ranges.

Finally, as an example test case, following the methodology of Gonzalez et al. (2023), where galaxy pairs are identified using z_p obtained with BCNz2, we have implemented the z_p galaxy catalogues determined with DEEPz in the W1+W3 fields with a precision of $\sigma_{68} = 0.01$. Based on the results of Gonzalez et al. (2023) and our own results, we have found a good agreement in the number of identified pairs and their physical properties. However, despite this agreement in number and physical properties, DEEPz and BCNz2 only match 40% of the total sample of galaxy pairs concerning the DEEPz sample, characterised by including photometric redshifts of nearby galaxies. Regarding the 60% of the pairs identified by DEEPz that are not found in the identification by BCNz2, we found that this difference is due to the low precision for distant galaxies by both methods, with BCNz2 having a greater error in these cases. Nevertheless, since all the galaxy pairs identified with redshifts provided by DEEPz and BCNz2 meet the purity and completeness criteria detailed in Rodriguez et al. (2020), we consider that the catalogues generated here are capable of identifying close galaxy pairs and that the combination of both methods improves their purity.

As future work, we note that the precision of DEEPz increases with more training examples. DEEPz shows biases from the spectroscopic surveys used in its training, and its precision is comparable to or better than BCNz2 in certain fields. These aspects and biases can be improved by including more spectroscopic information, which is time-consuming. Implementing data augmentation and sampling techniques could potentially solve this issue. This will be crucial to continue with transfer learning to improve DEEPz and make the models more general. This, in turn, allows for the expansion of the field of implementation of the catalogues for a more precise understanding of the Universe.

Acknowledgements

We would like to thank the Hanyue Guo for the useful comments and suggestions which has helped to improve this paper.

CosmoHub has been developed by the Port d'Informació Científica (PIC), maintained through a collaboration of the Institut de Física d'Altes Energies (IFAE) and the Centro de Investigaciones Energéticas, Medioambientales y Tecnológicas (CIEMAT) and the Institute of Space Sciences (CSIC & IEEC). CosmoHub was partially funded by the “Plan Estatal de Investigación Científica y Técnica y de Innovación” program of the Spanish government, has been supported by the call for grants for Scientific and Technical Equipment 2021 of the State Program for Knowledge Generation and Scientific and Technological Strengthening of the R+D+i System, financed by MCIN/AEI/10.13039/501100011033 and the EU NextGeneration/PRTR (Hadoop Cluster for the comprehensive management of massive scientific data, reference EQC2021-007479-P) and by MICIIN with funding from European Union NextGenerationEU (PRTR-C17.I1) and by Generalitat de Catalunya.

The PAU data centre is hosted by the Port d'Informació Científica (PIC), maintained through a collaboration of CIEMAT and IFAE, with additional support from Universitat Autònoma de Barcelona and ERDF. We acknowledge the PIC services department team for their support and fruitful discussions. This project has received funding from the European Union's Horizon 2020 Research and Innovation Programme under the Marie Skłodowska-Curie grant agreement No 734374 and HORIZON-MSCA-2021-SE-01 Research and Innovation programme under the Marie Skłodowska-Curie grant agreement number 101086388. This work was also partially supported by the Consejo Nacional de Investigaciones Científicas y Técnicas (CONICET, Argentina), Agencia Nacional de Promoción Científica y Tecnológica and the Secretaría de Ciencia y Tecnología de la Universidad Nacional de Córdoba (SeCyT-UNC, Argentina). This work has made use of CosmoHub. CosmoHub has been developed by the Port d'Informació Científica (PIC), maintained through a collaboration of the Institut de Física d'Altes Energies (IFAE) and the Centro de Investigaciones Energéticas, Medioambientales y Tecnológicas (CIEMAT), and was partially funded by the “Plan Estatal de Investigación Científica y Técnica y de Innovación” program of the Spanish government.

M. Eriksen acknowledges funding by MCIN with funding from European Union NextGenerationEU (PRTR-C17.I1) and by Generalitat de Catalunya. This work has been also partially supported by the Polish National Agency for Academic Exchange (Bekker grant BPN/BEK/2021/1/00298/DEC/1), the European Union's Horizon 2020 Research and Innovation programme under the Maria Skłodowska-Curie grant agreement (No. 754510). F. Rodriguez would like to acknowledge support from the ICTP through the Junior Associates Programme 2023-2028. C.M Baugh acknowledges support from the Science Technology Facilities Council through grant number ST/X001075/1. A. Wittje is supported by the DFG (SFB 1491). CIEMAT participation is supported by the grant PID2021-123012NB-C42P funded by MCIN/AEI/10.13039/501100011033. C. Padilla acknowledges support from the Spanish Plan Nacional project PID2019-111317GB-C32 and PID2022-141079NB-C32. P. Renard acknowledges the support by the Tsinghua Shui Mu Scholarship, the funding of the National Key R&D Program of China (grant no. 2023YFA1605600), the science research grants from the China Manned Space Project with No. CMS-CSST2021-A05, the Tsinghua University Initiative Scientific Research Program (No. 20223080023) and the National Science Foundation of China (grant no. 12350410365). J. Carretero acknowledges support from the grant PID2021-123012NA-C44 funded by MCIN/AEI/10.13039/501100011033 and by “ERDF A way of making Europe”. H. Hildebrandt is supported by a DFG Heisenberg grant (Hi 1495/5-1), the DFG Collaborative Research Center SFB1491, as well as an ERC Consolidator Grant (No. 770935). M. Siudek acknowledges support by the Polish National Agency for Academic Exchange (Bekker grant BPN/BEK/2021/1/00298/DEC/1), the State Research Agency of the Spanish Ministry of Science and Innovation under the grants 'Galaxy Evolution with Artificial Intelligence' (PGC2018-100852-A-I00) and 'BASALT' (PID2021-126838NB-I00). This work was partially supported by the European Union's Horizon 2020 Research and Innovation program under the Maria Skłodowska-Curie grant agreement (No. 754510).

Data Availability

The DEEPz photometric redshift catalogues in the W1, W3, and G09 fields will become publicly available on the CosmoHub plat-

form (Tallada et al. 2020; Carretero et al. 2017) in an upcoming data release at <https://cosmohub.pic.es/catalogs/319>. The data is currently available on a reasonable request to the author.

References

- Ade, P. A. R., Aghanim, N., Arnaud, M., et al. 2016, *Astronomy & Astrophysics*, 594, A13
- Aghanim, N., Ashdown, M., Aumont, J., et al. 2016, *Astronomy and Astrophysics*, 596
- Ahumada, R., Prieto, C. A., Almeida, A., et al. 2020, *The Astrophysical Journal Supplement Series*, 249
- Alarcon, A., Gaztanaga, E., Eriksen, M., et al. 2021, *The PAU Survey: An improved photo-z sample in the COSMOS field*
- Alarcon, A., Sánchez, C., Bernstein, G. M., & Gaztanaga, E. 2020, *Monthly Notices of the Royal Astronomical Society*, 498
- Baldry, I. K., Liske, J., Brown, M. J., et al. 2018, *Monthly Notices of the Royal Astronomical Society*, 474
- Barro, G., Pérez-González, P. G., Cava, A., et al. 2019, *The Astrophysical Journal Supplement Series*, 243
- Bellstedt, S., Driver, S. P., Robotham, A. S., et al. 2020, *Monthly Notices of the Royal Astronomical Society*, 496
- Benítez, N., Dupke, R., Moles, M., et al. 2014, in *Proceedings of the 11th Scientific Meeting of the Spanish Astronomical Society - Highlights of Spanish Astrophysics VIII*, SEA 2014
- Brammer, G. B., Van Dokkum, P. G., Franx, M., et al. 2012, *Astrophysical Journal, Supplement Series*, 200
- Carretero, J., Tallada, P., Casals, J., et al. 2017, in *Proceedings of the European Physical Society Conference on High Energy Physics*. 5-12 July, 488
- Castander, F. J., Ballester, O., Bauer, A., et al. 2012, in *Ground-based and Airborne Instrumentation for Astronomy IV*, Vol. 8446
- Castander, F. J., Serrano, S., Eriksen, M., et al. 2024, *Arxiv*
- Cenarro, A. J., Moles, M., Cristóbal-Hornillos, D., et al. 2019, *Astronomy and Astrophysics*, 622
- Childress, M. J., Lidman, C., Davis, T. M., et al. 2017, *Monthly Notices of the Royal Astronomical Society*, 472
- Conroy, C. & Gunn, J. E. 2010, *Astrophysical Journal*, 712
- Conroy, C., Gunn, J. E., & White, M. 2009, *Astrophysical Journal*, 699
- Csizi, B., Tortorelli, L., Siudek, M., et al. 2024, *Arxiv*
- Davies, L. J., Driver, S. P., Robotham, A. S., et al. 2015, *Monthly Notices of the Royal Astronomical Society*, 447
- De Jong, J. T., Verdoes Kleijn, G. A., Boxhoorn, D. R., et al. 2015, *Astronomy and Astrophysics*, 582
- de Jong, J. T., Verdoes Kleijn, G. A., Kuijken, K. H., & Valentijn, E. A. 2013, *Experimental Astronomy*, 35
- De Oliveira, C. M., Ribeiro, T., Schoenell, W., et al. 2019, *Monthly Notices of the Royal Astronomical Society*, 489
- DESI Collaboration, Adame, A. G., Aguilar, J., et al. 2024, *Arxiv*
- Dressler, A., Bigelow, B., Hare, T., et al. 2011, *Publications of the Astronomical Society of the Pacific*, 123
- Driver, S. P., Davies, L. J., Meyer, M., et al. 2016, in *Astrophysics and Space Science Proceedings*, Vol. 42
- Driver, S. P., Hill, D. T., Kelvin, L. S., et al. 2011, *Monthly Notices of the Royal Astronomical Society*, 413
- Driver, S. P., Norberg, P., Baldry, I. K., et al. 2009, *Astronomy and Geophysics*, 50
- Edge, A., Sutherland, W., Kuijken, K., et al. 2013, *The Messenger*, 154
- Erben, T., Hildebrandt, H., Miller, L., et al. 2013, *Monthly Notices of the Royal Astronomical Society*, 433
- Eriksen, M., Alarcon, A., Cabayol, L., et al. 2020, *Monthly Notices of the Royal Astronomical Society*, 497
- Eriksen, M., Alarcon, A., Gaztanaga, E., et al. 2019, *Monthly Notices of the Royal Astronomical Society*, 484
- Garilli, B., Guzzo, L., Scoddeggio, M., et al. 2014, *The VIMOS public extragalactic survey (VIPERS) : First data release of 57 204 spectroscopic measurements*
- Garilli, B., McLure, R., Pentericci, L., et al. 2021, *The VANDELS ESO public spectroscopic survey: Final data release of 2087 spectra and spectroscopic measurements*
- Geha, M., Wechsler, R. H., Mao, Y.-Y., et al. 2017, *The Astrophysical Journal*, 847
- Gonzalez, E. J., Rodriguez, F., Navarro-Gironés, D., et al. 2023, *Monthly Notices of the Royal Astronomical Society*, 522
- Guzzo, L., Scoddeggio, M., Garilli, B., et al. 2014, *Astronomy and Astrophysics*, 566
- Heymans, C., Van Waerbeke, L., Miller, L., et al. 2012, *Arxiv*
- Hildebrandt, H., Arnouts, S., Capak, P., et al. 2010, *Astronomy and Astrophysics*, 523
- Hildebrandt, H., Erben, T., Kuijken, K., et al. 2012, *Monthly Notices of the Royal Astronomical Society*, 421
- Hopkins, A. M., Driver, S. P., Brough, S., et al. 2013, *Monthly Notices of the Royal Astronomical Society*, 430
- Hoyle, B., Gruen, D., Bernstein, G. M., et al. 2018, *Monthly Notices of the Royal Astronomical Society*, 478
- Jarrett, T. 2004, *Publications of the Astronomical Society of Australia*, 21, 396
- Johnston, H., Joachimi, B., Norberg, P., et al. 2021, *The PAU Survey: Intrinsic alignments and clustering of narrow-band photometric galaxies*
- Krzywinski, M. & Altman, N. 2014, *Nature Methods*, 11
- Kuijken, K., Heymans, C., Hildebrandt, H., et al. 2015, *Monthly Notices of the Royal Astronomical Society*, 454
- Le Fèvre, O., Cassata, P., Cucciati, O., et al. 2013, *Astronomy and Astrophysics*, 559
- Lilly, S. J., Le Brun, V., Maier, C., et al. 2009, *Astrophysical Journal, Supplement Series*, 184
- Liske, J., Baldry, I. K., Driver, S. P., et al. 2015, *Monthly Notices of the Royal Astronomical Society*, 452
- Manzoni, G., Baugh, C. M., Norberg, P., et al. 2024, *Monthly Notices of the Royal Astronomical Society*, 530
- Martí, P., Miquel, R., Bauer, A., & Gaztañaga, E. 2014, *Monthly Notices of the Royal Astronomical Society*, 437
- Masters, D. C., Stern, D. K., Cohen, J. G., et al. 2019, *The Astrophysical Journal*, 877
- McGill, R., Tukey, J. W., & Larsen, W. A. 1978, *American Statistician*, 32
- Mesa, V., Duplancic, F., Alonso, S., Coldwell, G., & Lambas, D. G. 2014, *Monthly Notices of the Royal Astronomical Society*, 438
- Molino, A., Benítez, N., Moles, M., et al. 2014, *Monthly Notices of the Royal Astronomical Society*, 441
- Molino, A., Costa-Duarte, M. V., Sampedro, L., et al. 2020, *Monthly Notices of the Royal Astronomical Society*, 499
- Nanayakkara, T., Glazebrook, K., Kacprzak, G. G., et al. 2016, *The Astrophysical Journal*, 828
- Navarro-Gironés, D., Gaztañaga, E., Croce, M., et al. 2023, *Arxiv*
- Newman, J. A., Cooper, M. C., Davis, M., et al. 2013, *Astrophysical Journal, Supplement Series*, 208
- Padilla, C., Castander, F. J., Alarcón, A., et al. 2019, *The Astronomical Journal*, 157
- Pickles, A. 1998, *Publications of the Astronomical Society of the Pacific*, 110
- Renard, P., Siudek, M., Eriksen, M. B., et al. 2022, *Monthly Notices of the Royal Astronomical Society*, 515
- Rodriguez, F., Gonzalez, E. J., O'Mill, A. L., et al. 2020, *Astronomy and Astrophysics*, 634
- Salvato, M., Ilbert, O., & Hoyle, B. 2019, *The many flavours of photometric redshifts*
- Schlegel, D. J., Finkbeiner, D. P., & Davis, M. 1998, *The Astrophysical Journal*, 500
- Serrano, S., Gaztañaga, E., Castander, F. J., et al. 2022, *Arxiv*
- Steidel, C. C., Rudie, G. C., Strom, A. L., et al. 2014, *Astrophysical Journal*, 795
- Sullivan, M., Conley, A., Howell, D. A., et al. 2010, *Monthly Notices of the Royal Astronomical Society*, 406
- Survey, D. E., Collaboration, K.-D. S., et al. 2023, *Arxiv*
- Tallada, P., Carretero, J., Casals, J., et al. 2020, *Astronomy and Computing*, 32, 100391
- Tanaka, M. & Kodama, T. 2004, in *Proceedings of Science*, Vol. 2004-October
- Taniguchi, Y., Kajisawa, M., Kobayashi, M. A., et al. 2015, *Publications of the Astronomical Society of Japan*, 67
- Toomre, A. & Toomre, J. 1972, *The Astrophysical Journal*, 178
- Tortorelli, L., Siudek, M., Moser, B., et al. 2021, *Journal of Cosmology and Astroparticle Physics*, 2021
- Van Den Busch, J. L., Wright, A. H., Hildebrandt, H., et al. 2022, *Astronomy and Astrophysics*, 664
- Venemans, B. P., Verdoes Kleijn, G. A., Mwebaze, J., et al. 2015, *Monthly Notices of the Royal Astronomical Society*, 453
- Weinberg, D. H., Mortonson, M. J., Eisenstein, D. J., et al. 2013, *Observational probes of cosmic acceleration*

Appendix A: Feature selection

One of the most important steps in classifier determination is generating and selecting the features with the highest entropy. To do this, we implemented different statistical methods, particularly unsupervised learning and univariate analysis. In Fig. A.1, we show in the left panel the heat map of the different Pearson correlations between the bands, and in the central and right panels, the scores obtained applying the mutual information and regression methods, respectively. This type of analysis allows us to estimate the importance of the features, i.e., the bands for the analysis or modeling, and to discard irrelevant or redundant ones. Reducing the number of features while preserving the most important information improves the efficiency and interpretation of the models. We observe that the trend of the BBs is similar to the trend of the NBs in terms of importance when studying their relationship with the spectroscopic redshift intervals, so it is interesting to study the necessity of the BBs. Additionally, we note that the regression method assigns a lower score to the bands of blue wavelengths compared to the rest of the bands, so it is interesting to study their importance in determining the z_p .

Appendix B: Performance for field and refinement data test

Each row corresponds to a different refinement test for the five samples. In the left column, the results are presented according to 10 i -band bins, while in the right column, the results are shown according to 10 z_s bins. Each result is linked to the initial training and validation samples within each field and its combination; these samples may increase, decrease, or remain constant in the number of examples, depending on the refinement data test being conducted. Therefore, the intervals in each curve of each figure vary. The different data refinement tests are showed in Fig. B.1 and are summarised in the heatmap of Fig. B.2, this plots are showing the value of the σ_{68} metric for the validation sample.

In general, we find that σ_{68} as a function of i and z_s varies in the same way as seen in the Sect. 4 for the baseline samples. However, this behaviour is not observed for the G09 field. This is because the samples from the G09 field have spectroscopic information restricted up to $i = 20.5$ and $z_s = 0.6$, i.e., it considers only bright galaxies. Therefore, in this field, lower values are generally observed in the metrics compared to other samples.

Appendix C: Extrapolation to other regions of the sky

In this appendix we study the impact of applying DEEPz on sky regions not included in the training set. Specifically, we test how the performance changes if being trained in W1 and validated in W3 or vice versa. In Fig.C.1, you can see σ_{68} as a function of the i -band magnitude, photo- z , and spectroscopic redshift.

The trends shown in Fig. C.1, when the training and validation samples match, are consistent with those seen in Fig. 3 and Fig. B.2. A higher precision is observed in the W1 field compared to the W3 field, with a slight deterioration when the validation samples are swapped between these two fields. However, this decrease is more pronounced when DEEPz is trained exclusively with galaxies from the W3 field and applied to galaxies from the W1 field. Based on these trends, it is likely that performance in new fields will vary slightly in new regions.

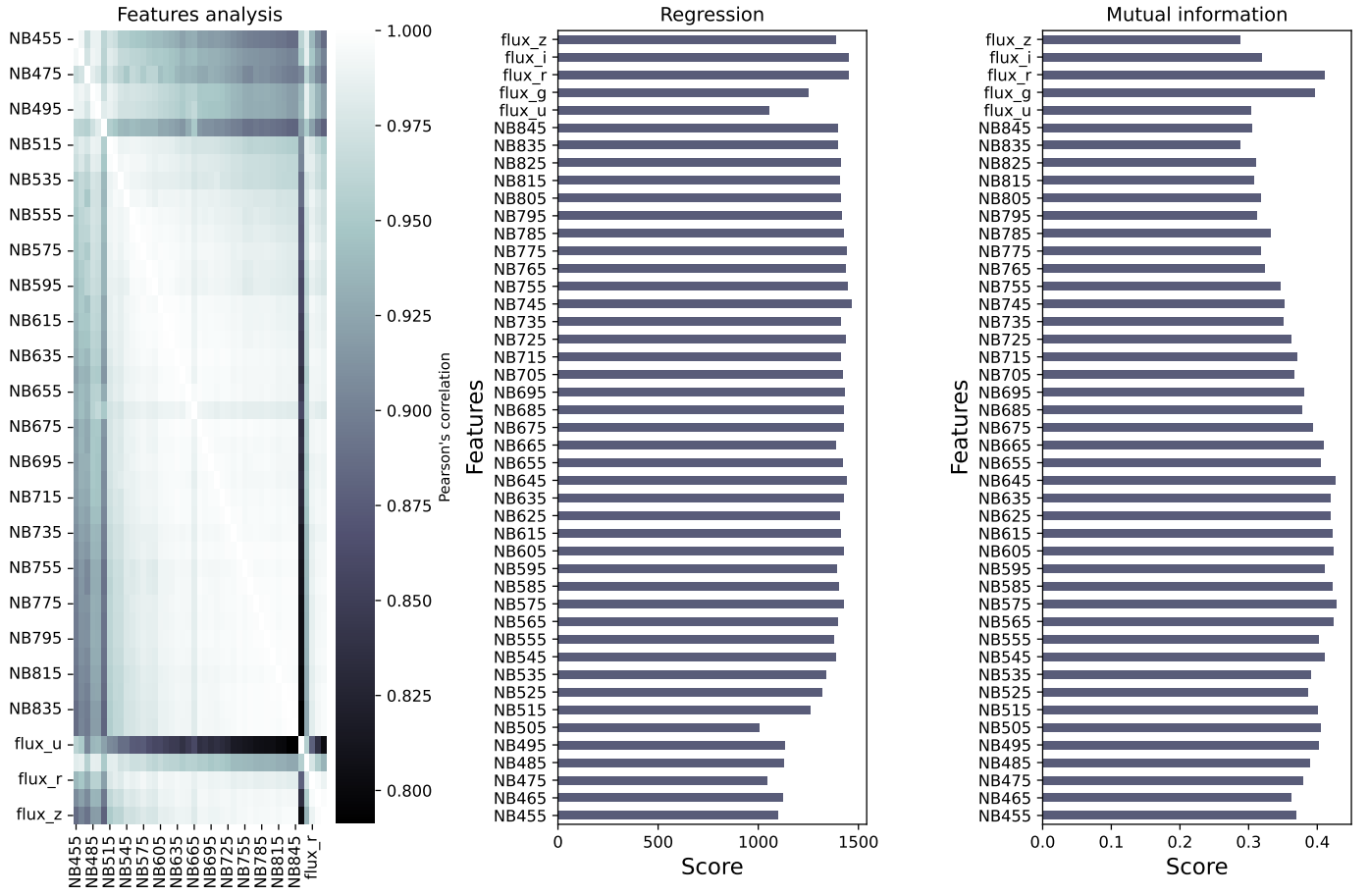


Fig. A.1. Visualisation of univariate study of bands used in W1 and W3 fields. *Left panel:* correlation among the bands through Pearson correlation. *Central panel and right panel:* Bar chart of the scores of the correlated bands with the spectroscopic redshift bins calculated through MI and regression methods.

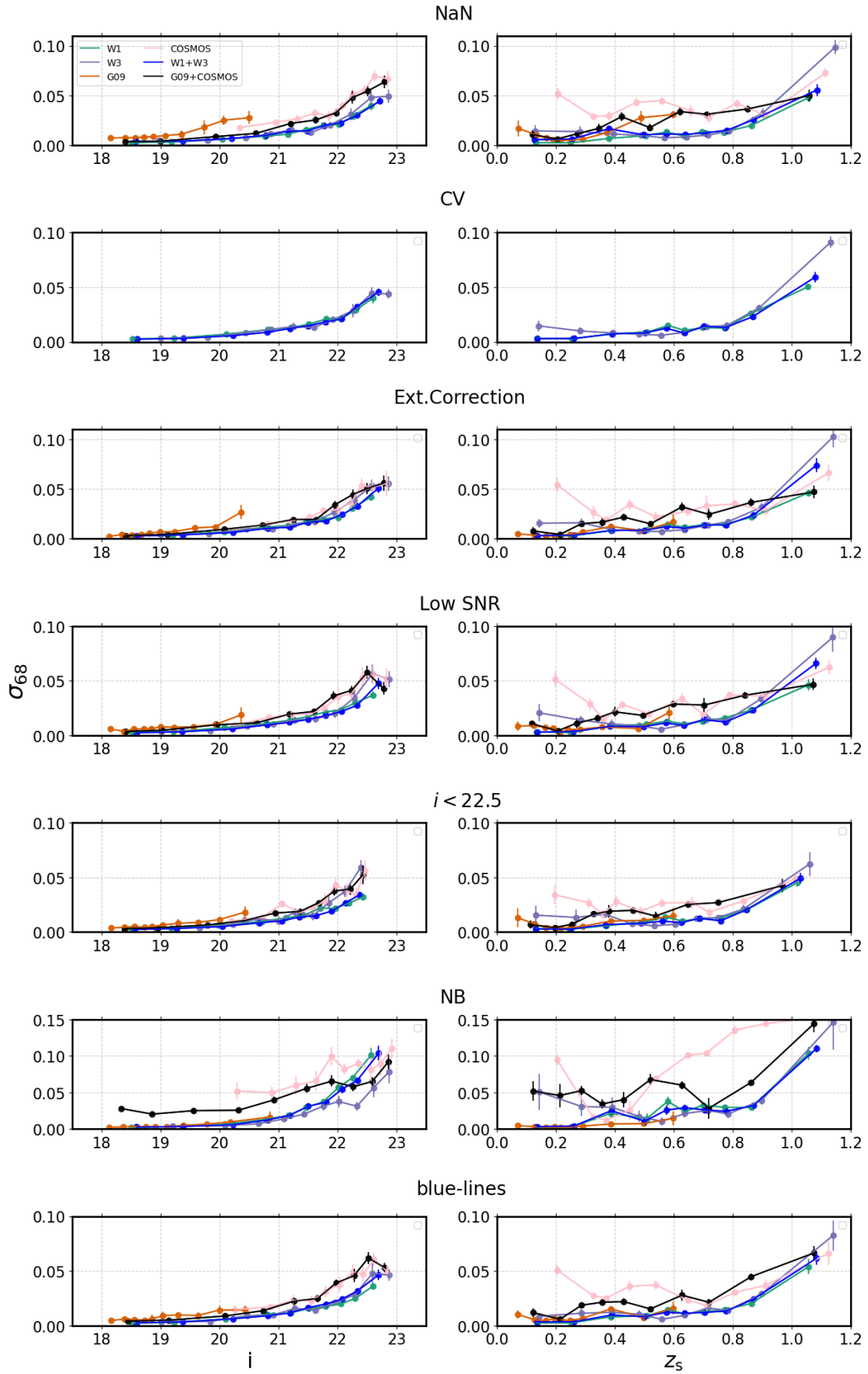


Fig. B.1. Trend of σ_{68} as a function of the i -band magnitude and spectroscopic redshift for each field and the combination W1+W3 and G09+COSMOS. Each row corresponds to a data refinement study, hence the validation sets are different.

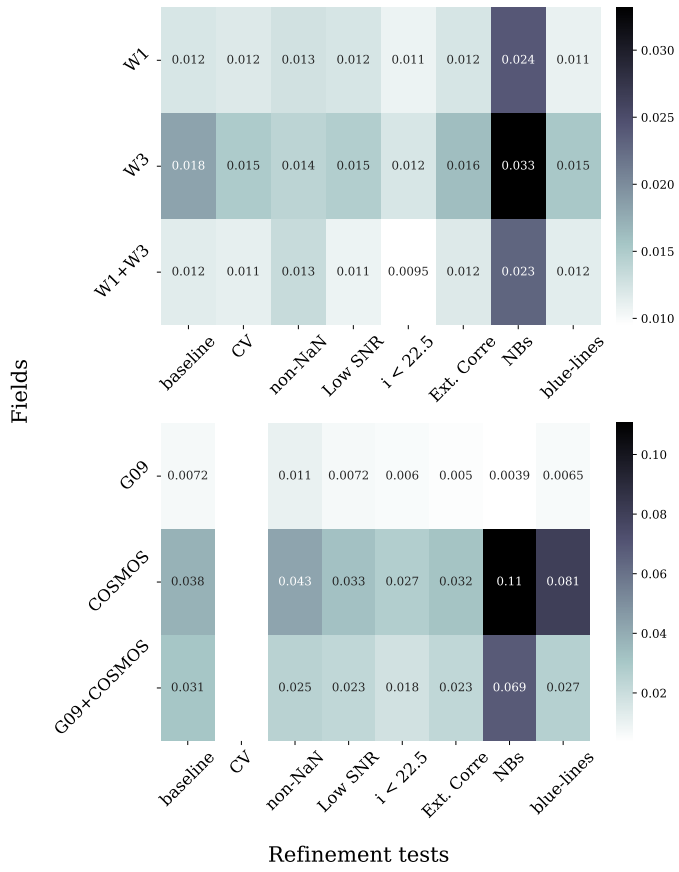


Fig. B.2. Heatmaps of σ_{68} from the validation sample of each study. *Top panel:* Galaxy samples in W1, W3, and W1+W3 combined. *Bottom panel:* Galaxy samples in G09, COSMOS, and G09+COSMOS combined.

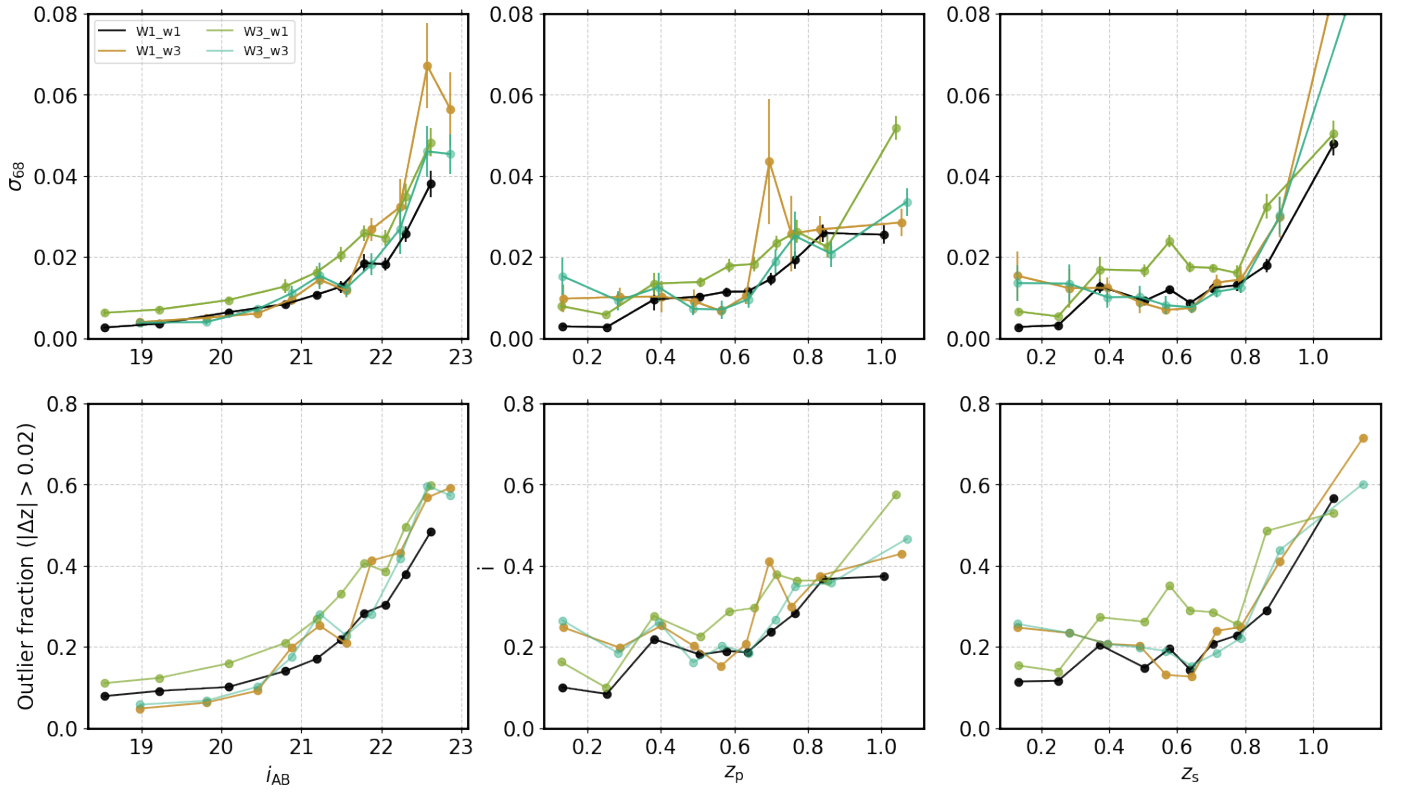


Fig. C.1. Trends in the measurement of σ_{68} . The distribution is divided into ten bins, each containing the same number of objects, based on the apparent magnitude in the i -band and z_s , in the left and right columns, respectively. These trends show the precision, in terms of the centralised scatter σ_{68} , in the W1 and W3 validation sets. The solid line represents when the training and validation samples coincide, and the dashed line indicates training with W1 and validation with W3, or vice versa.